THESIS FOR THE DEGREE OF LICENTIATE OF ENGINEERING

A Realizable Hybrid Mixture-Bubble Model for Cavitating Flows

EBRAHIM GHAHRAMANI

A Realizable Hybrid Mixture-Bubble Model for Cavitating Flows

EBRAHIM GHAHRAMANI

A Realizable Hybrid Mixture-Bubble Model for Cavitating Flows

EBRAHIM GHAHRAMANI
Department of Mechanics and Maritime Sciences
Chalmers University of Technology

Abstract

Cavitating multi-phase flows include an extensive range of cavity structures with different length scales, from micro bubbles to large sheet cavities that may fully cover the surface of a device. To avoid high computational expenses, incompressible transport equation models are considered a practical option for simulation of large scale cavitating flows, normally with limited representation of the small scale vapour structures. To improve the resolution of all scales of cavity structures in these models at a moderate additional computational cost, a possible approach is to develop a hybrid Eulerian mixture - Lagrangian bubble solver in which the larger cavities are considered in the Eulerian framework and the small (sub-grid) structures are tracked as Lagrangian bubbles. In this thesis, such a multi-scale model for simulation of cavitating flows is being developed. In the current report, first the performance of three different numerical approaches in cavitation modelling are compared by studying two benchmark test cases to understand the capabilities and limitations of each method. Two of the methods are the well established compressible thermodynamic equilibrium mixture model and the incompressible transport equation finite mass transfer (FMT) mixture model, which are compared with a third method, a recently developed Lagrangian discrete bubble model. In the Lagrangian bubble model, the continuum flow field is treated similar to the FMT approach, however the cavities are represented by individual bubbles. After describing the aforementioned cavitation models, the hybrid mixture-bubble model is presented with a discussion over some of the encountered numerical issues in the model development. This model is developed by coupling the Eulerian FMT mixture model and the Lagrangian bubble model in the open source C++ package OpenFOAM. A critical step in developing this hybrid model is the correct transition of the cavity structures from an Eulerian to a Lagrangian framework. To address these issues, a new improved formulation is developed, and simulation results are presented that shows the issues are overcome in the new model. Further, for the Lagrangian modelling, different ways to consider how the fluid pressure influences bubble dynamics are studied, including a novel way by considering the local pressure effect in the Rayleigh-Plesset equation, which leads to improved predictions.

Keywords: Cavitation, Eulerian-Lagrangian model, Disperse multiphase flow, Multi-scale model, Homogeneous mixture model, OpenFOAM

Acknowledgement

CONTENTS

LIST OF FIGURES

LIST OF TABLES

1

Introduction

1.1 Cavitation

Cavitation is a common phenomenon in industrial hydraulic systems, such as marine propulsion systems, turbines and fuel injectors. It is in many cases undesirable and it is tried to avoid its occurrence, or at least to minimize its effects. One issue is material loss and degradation of the hydraulic systems due to cavitation erosion, which is believed to be the result of violent and very fast collapses of the generated vapour micro-bubbles. Moreover, cavitation is often accompanied by issues of noise, vibrations, load variations, blockage and loss of efficiency in hydraulic devices. However, it is found a desirable event in some other situations such as ultrasonic cleaning and ultrasonic drug delivery. Therefore, reliable prediction and control of cavitation is of considerable importance in the design of hydraulic and marine systems as well as its application in biomedical treatment and chemical systems.

1.1.1 Definition

Cavitation is the formation of vapour in a liquid when local static pressure of liquid falls below a critical pressure threshold. As pressure of a larger region gets below the threshold pressure, more liquid will change phase into vapour. Without considering the effects of shear forces in flowing fluids, the pressure threshold is equal to the saturation pressure. The difference between cavitation and boiling is that cavitation occurs due to pressure drop while boiling is caused due to an increase in temperature.

The region or pocket of the generated vapour in the cavitating flows is called cavity. The cavity can be either steady and attached to the surface or it can be separated from the surface and transported downstream. Multiphase cavitating flows contain an extensive range of cavity structures with different length scales. For example, a sheet cavity that fully or partially cover the suction side of a hydrofoil

may break down into smaller cloud cavities and micro bubbles which are further transported into regions of higher pressure, where collapse-like condensation results in the formation of liquid jets and pressure shocks. Due to the mentioned significance and complexity of the flow field, understanding and controlling cavitation has been a major challenge in engineering in recent decades and various numerical and experimental approaches have been developed for different applications.

1.2 Numerical simulation

Computational Fluid Dynamics (CFD) simulation, which can be a supplement or alternative to experimental measurements, have gained more popularity in recent decades. Experimental tests can be very expensive, suffer from scale effects, and give limited information; the latter is a particular problem in cavitating flows where the application of optical measurement techniques is often not possible. In comparison, CFD methods can provide more detailed features of the flow field to have a more comprehensive understanding of the hydrodynamics of cavitation. However, cavitating flows include a vast range of spatial and temporal scales in different applications, and sometimes are accompanied by other processes and flow effects that makes the modelling and computations challenging. For example, the duration of the final stage of bubble or cavitating vortex collapse is of the order of one microsecond [1] while the erosion process might take place over the lifetime of a propeller. Also, the normal velocity of the interface can vary from some meters per second for turbomachinery systems to hundreds of meters per second in diesel injector nozzles. Besides that, the peak pressures can reach up to several thousands of bars for a few microseconds during the last stages of cavity collapse. Another parameter to consider is fluid properties, as cavitation does not occur only in water but also in e.g. rocket pumps, the lubricant of bearing [2], diesel injectors, or blood vessels during ultrasound drug delivery. Depending on the fluid properties and pressure differences, sometimes strong shock waves and considerable temperature variations are seen in the domain which means that compressibility and thermal effects should be considered in the simulation. Considering the issues with sufficient spatial and temporal resolutions as well as the mentioned flow effects, there is no unique CFD approach today that has sufficient performance for all cavitation problems. In fact, current computational capabilities do not allow the resolution of all scales arising in typical cavitating flows except for a few academic cases [3]. Therefore, various numerical methods are being used today, and each of them is applicable or feasible only to a specific group of cavitation problems. There are different categorizations of cavitation models based on the fundamental assumptions behind them.

1.2.1 Equilibrium models

In one group of models, the two-phase cavitation regime is considered as a single fluid flow which is in mechanical and thermodynamic equilibrium. This equilibrium assumption implies that mass transfer rate at the gas-liquid interface is infinite. These models are mostly implemented in density-based algorithms with different approaches to find the pressure-density relation. For example, Schnerr at al. [4] and Koop [2] used an equation of state (EoS) to find the flow pressure. The different phases and their relevant interface are recognised based on the density value at each point and the EoS can be a function of temperature. Kyriazis et al. [5] used an explicit density-based solver with real fluid thermodynamic properties for n-Dodecane to demonstrate heating effects in bubble collapse cases. When the flow temperature variation is not significant, the EoS can be independent of the temperature which simplifies the pressure-density relations; this is known as barotropic EoS. The barotropic models are implemented in both density-based (e.g. Koukouvinis et al. [6]) and pressure-based algorithms. Goncalves et al. [7] compared an incompressible pressure-based solver with a compressible density-based solver with barotropic cavitation models. From the results it seems necessary to consider fluid compressibility effects to correctly describe the cavity dynamics. The single fluid EoS models do not usually need any empirical parameters; however the captured liquid-gas interface is rather diffuse in these models and a high grid resolutions with very small time steps are needed for adequate prediction of a sharp interface. Furthermore, to correctly capture pressure wave propagation, very small time steps are normally needed in the simulation. Therefore, these models are computationally expensive and they are usually applied to cavitating flows in small scale geometries such as diesel injector nozzle flows.

1.2.2 Transport equation based models

Another widely used modelling approach is the transport equation based method. Here, similar to the previous approach, the multiphase flow is treated as a homogenous mixture and one set of continuity and momentum equation is used to calculate the mixture flow. However, a transport equation is solved to capture the liquid-vapour interface. This equation can be developed based on the volume fraction of the two phases (e.g. Singhal [8] and Bensow and Bark [9]) or through a level-set method, i.e. expressed based on a signed distance of any point to the interface, e.g. [10]. Also, the mass transfer between the phases is defined as an explicit source term to the transport equation. Therefore, this approach, known as finite mass transfer rate method (FMT), should incorporate a numerical model to estimate vaporization and condensation rates. Most models that are used in the literature (selectively [11], [12] and [13]) estimate the phase change rate based on a simplified form of the Rayleigh-Plesset equation, in which the second temporal derivative of bubble radius as well as the effect of non-condensable gas are ignored. This simplification may affect the model accuracy; Ye and Li [14] showed that the bubble growth rate can become greatly reduced if the bubble-bubble in-

teraction and second-order derivative in the Rayleigh-Plesset equation are considered. To improve the model accuracy, however, some empirical constants are implemented in these models which should be tuned for each different simulation to adjust the mass transfer rate. Such uncertainty of model constants is one of the limitations of the finite mass transfer approach. A recent study by Koukouvinis and Gavaises [15] showed that even with the finite mass transfer approach consistent results can be achieved by theoretically increasing the transfer rates to infinity. The transport equation method is commonly implemented in pressure-based algorithms and the pure fluids are usually assumed to be incompressible; there are however a few studies in which the fluid compressibility is taken into account. For example, Koukouvinis et al. studied the expansion and collapse of a single bubble subject to gravity [16] and in the vicinity of a free surface [17]. However, they ignored the mass transfer rate in the simulation. Also, Yakubov et al. [18] investigated the effect of fluid compressibility in pressure-based solvers using the finite mass transfer approach. This study shows that considering fluid compressibility in the pressure correction equation may lead to ill-conditioned matrices of coefficients which can cause numerical issues for steady-state simulations or transient simulations with large time steps. From the results, it can also be inferred that the cavitation patterns are very similar for compressible and incompressible simulations. Therefore, for the large scale problems, such as cavitating ship propellers and turbines, it is more common to use incompressible transport equation models as they are less computationally expensive and can give rather satisfactory results using larger time steps, as compared to equilibrium-based models. However, due to simplifications in the mass transfer rate model as well as the grid resolution dependency of the transport equation, cavity structures smaller than the grid size, such as cavitation nuclei and bubbles, or sparse clouds of bubbles, are not well treated using these approaches. Accurate simulation of such structures and their violent collapse and fast rebounds are very important in accurate prediction of cavitation erosion.

1.2.3 Discrete bubble model

Discrete bubble model (DBM) is an approach in which the cavity structures are tracked in a Lagrangian framework while the continuum flow is calculated using Eulerian governing equations. In other words, cavity structures are considered as individual bubbles and groups of bubbles, or parcels of them, and tracked by solving the Lagrangian equations of motion. Different numerical studies in the literature show the potential of this method to represent cavitation phenomenon. Giannadakis et al. [19], for example, studied the predictive capability of a stochastic Lagrangian model accounting for the onset and development of cavitation inside diesel nozzle holes. Since different flow forces on cavities are implemented directly in the transport equation and bubble size variation is represented using a more accurate form of the Rayleigh-Plesset equation, the Lagrangian approach can give a more realistic estimation of cavitation dynamics as compared to the

transport equation approach. Abdel-Maksoud et al. [20] compared Eulerian and Lagrangian methods, and showed that only Lagrangian models are able to describe correctly the bubble behaviour in vortices. In this method, the small sub-grid scale structures and nuclei can be resolved which is crucial in cavity collapse and rebound estimation as well as erosion prediction. Also, it allows to take into account inhomogeneous and transient water-quality effects [21].

To have a more physical representation of the cavity dynamics in DBM, various interactions between cavity structures should be modelled appropriately in the solution algorithm. These interactions include, but are not limited to, different flow forces on bubble trajectory as well as its dynamic, turbulence effect on bubble motion and break-up, bubble-bubble interaction and the bubble contribution on mixture properties and surrounding pressure. However, the Lagrangian models can be computationally expensive when the number of bubbles is large. Besides that, they are limited in representation of large and non-spherical vapour structures.

1.2.4 Hybrid models

Considering the stated limitations of the previous groups, there is no numerical model in these categories which is capable in resolving all spatial and temporal scales in a general cavitating flow. However, from the above mentioned capabilities of the Eulerian and Lagrangian formulations, a solution can be to develop a hybrid multi-scale model to resolve the large vapour structures through a mixture approach, and to capture the small-scale structures as discrete bubbles (e.g. [22]).

Using multi-scale models to simulate multiphase flows is a popular approach and numerous studies can be found in literature. For example, Tomiyama and Shimada [23] proposed a (N+2)-field modeling approach which can deal with two continuous phase fields and N dispersed gas phase fields. Also, Černe et al. [24] and Štrubelj and Tiselj [25] developed another model by coupling of an interface capturing Volume of Fluid (VOF) based method with the two-fluid model, so that in the parts of the domain where the flow was too dispersed to be described by the interface capturing algorithms, the two-fluid model was used. However, as explained before, Eulerian approaches are limited in capturing small sub-grid bubble dynamics with reasonable computational expense and most of the developed multi-scale models in literature are Eulerian-Eulerian solvers. The concept of multi-scale hybrid Eulerian-Lagrangian solvers is a more recent approach to simulate multiphase flows in large scale applications for which effective small scale details need to be resolved sufficiently. This methodology has gained more popularity in recent years for simulation of atomizing gas-liquid flows [26]. The works of Kim et al.[27], Herrmann [28] and Tomar et al. [29] are the pioneering efforts to couple the Lagrangian Particle Tracking (LPT) with transport equation based methods. Also, Ling et al. [30] developed a hybrid model with more emphasis on the correction of momentum equation source terms due to the Eulerian-Lagrangian coupling in order to accurately compute the dynamics of the

Lagrangian droplets that are larger than the grid spacing. In that study, the Eulerian structures are directly converted to one Lagrangian droplet with equal volume (similar to Tomar et al. [29]), but only a special zone of the flow domain is subjected to this conversion and thin ligaments and sheets are exempted from this treatment. In addition to the direct transition from Eulerian to Lagrangian structures, there are statistical algorithms (e.g. [31]) in which the transfer of mass from Eulerian to Lagrangian framework is done via a statistical model, tuned to the upstream predictions of the Eulerian model. This method reduces the computational time in comparison to the previous method, but some of the information (positions, mass, momentum) may not be preserved during the transition. Also, Ström et al. [32] used a switching zone with a statistical method which is designed to ensure that the Lagrangian parcels exit the zone with the correct statistics. The advantage of this approach was that the computationally demanding resolution of the liquid primary atomization process could be avoided altogether.

The mentioned Eulerian-Lagrangian hybrid models have been developed for atomizing gas-liquid flows, however, this approach can be utilized for cavitating flows as well. For example, Hsiao et al. [33] and Ma et al. [34] have developed a model with coupling of a Lagrangian Discrete Singularities Model and an Eulerian level set approach. In these studies, the Eulerian cavities are directly transformed to Lagrangian bubbles, but the bubble volume is spread smoothly over neighbouring cells within a selected radial distance. There are important distinctions between cavitating flow and atomizing flow applications which should be considered in model developments. In the mentioned hybrid models for atomizing flows (except [32]), it has been assumed that the Lagrangian particles do not occupy any volume in the Eulerian description which is valid when the Lagrangian formulation is used only in the dilute regions of a flow. Also, the resulting model will be useful in situations where continuous phase density is very low in comparison to the dispersed phase density [32], such as liquid spray applications. However, in cavitating flows we encounter the opposite case since the continuous phase density (water) is much larger than the (vapour) bubble density and such an assumption is not valid. Besides that, in liquid atomizers the dilute dispersed flow region and continuous two-phase region are present in separate regions of the flow as the dispersed droplets are results of the break-up of the two-phase structures in the downstream, this makes the numerical implementation of the transition algorithm more convenient. However, in cavitating flows, at each point of the two-phase regime, both small bubbles as well as large Eulerian cavities can be present. Another significant difference between the two applications is that in atomized liquids, for direct transition each liquid fragment is usually converted into one Lagrangian droplet with equal volume, while in cavitating flows, each Eulerian structure is actually a cloud of bubbles or a bubbly mixture and its properties (e.g. density) are not equal to the pure vapour (dispersed phase) properties. Therefore, the cavity might be replaced by a group of smaller bubbles (instead of one larger bubble) in such a way that the properties of the combined bubble group are equal to the corresponding values of the old Eulerian cavity.

Vapour condensation / liquid vaporization is a mass transfer process which only happens in the cavitating flows, adding the need for modelling mass transfer in the governing equations. A key factor in developing such solvers is the correct and smooth transition between Lagrangian and Eulerian structures and it is more important in cavitating flow simulations. When an Eulerian mixture structure is transformed to a Lagrangian bubble or vice versa, since the related transport equation to track the structure is modified, a wrong transition process may cause drastic non-continuous changes and spurious numerical pulses in the domain.

1.3 Objectives of the study

Considering the described capabilities and limitations of different models in the previous section, the main objective of this study is to develop a hybrid mixture-bubble model in OpenFOAM that is capable in representing cavitation phenomenon with extensive range of length scales from large sheet and cloud cavities that may fully cover a device surface to sub-grid micro bubbles. To fulfil this objective, the following steps have been taken in this thesis.

- Development of a discrete bubble cavitation model in OpenFOAM: There is no Lagrangian cavitation model in the OpenFOAM code, and the first step is to develop such a model by implementing a basic available Lagrangian library in a suitable continuum flow solver in the code. Then, the Lagrangian library needs to be improved to solve for the bubble dynamics and consider the bubble effect on the continuum flow field. A necessary step in this part is to improve the general Rayleigh-Plesset equation in determining the cavitation bubble dynamics. Other improvements in this part are correcting the bubble-wall boundary condition in OpenFOAM and considering the bubble-bubble interaction on bubble dynamics.

- Comparing different cavitation models: A general description of the limitations of different models is given in the previous section. However, to have a further understanding of each model behaviour and finding the potential area of improvements for the Eulerian and Lagrangian parts of the hybrid model, the performance of the three types of the cavitation models, i.e. EoS, FMT and DBM models, should be compared in the simulation of benchmark test cases. It also verifies the implementation of the DBM model in OpenFOAM.

- Coupling of the Eulerian mixture model with the Lagrangian bubble model: To develop the main hybrid solver, the DBM and FMT models should be coupled in OpenFOAM and a transition criterion should be defined to transform the small collapsing cavities from the Eulerian framework to the Lagrangian one and also to transform large Lagrangian structures to the Eulerian framework. This step is similar to the work of Vallier [35], in turn inspired by the study of Tomar et al. [29].

- Realizable improvement of the hybrid mixture-bubble model: As will be explained in the following chapters, after coupling the mixture and bubble models, the first solver that is developed based on available models in literature, need to be improved further to have a physically compatible transition between Eulerian and Lagrangian frameworks, and to consider the bubble contribution in the continuum flow field and mixture properties. Such improvements are another contribution of the current study.

1.4   Thesis outline

In chapter 2, the different numerical models that are used in this study are described. First, the three models from different approaches (§1.2.1- §1.2.3) are introduced. Then the coupling of an Eulerian model with a Largangian method in the hybrid solver is explained in detail, with focus on the correct definition of the transition process and the improved Eulerian governing equations.

In Chapter 3, the performance of the first three models are compared in simulating two benchmark test cases. This comparison helps to identify and understand the capabilities and limitations of each group of numerical models. The first test case is the single bubble collapse. For this case, an analytical solution is available, and the predicted bubble collapse behaviour and the surrounding pressure can be assessed in detail. In this part, the effects of different parameters such as mass transfer model empirical constant (used in the finite mass transfer and Lagrangian models), as well as spatial and temporal resolutions in capturing the flow physics are investigated. After that, the models are compared in simulating the collapse of a cluster of bubbles, previously studied by Schmidt et al.[36]. Here, no exact solution is available but only comparison between the methods can be made. In the bubble cluster, the effect of neighbouring bubbles and relative pressure pulses play an important role in the collapse behaviour. In addition to validating the Lagrangian model and the improved form of the Rayleigh-Plesset equation, the performance of the Eulerian finite mass transfer model is studied in detail and the effect of various parameters in this method including empirical constants are investigated, which helps to have a better understanding of its behaviour and possible source of deficiencies for future improvements. In the these two cases, the emphasise is on the Lagrangian model performance in prediction of bubble collapse dynamics and its effect on the continuum pressure.

In the last section of chapter 3, different cavity patterns over a two dimensional hydrofoil is simulated to present the overall performance of the hybrid model and also to validate the improved Eulerian-Lagrangian transition process. The report is then concluded with recommendations for future improvements of finite mass transfer and Lagrangian models as well as introducing the ongoing plan in further development of the hybrid solver.

A part of this work is published in one journal article [37] and another part is submitted for another article in the International Journal of Multiphase Flows.

2

Numerical methods

In this study, a hybrid solver is developed through the coupling of an Eulerian volume fraction based mixture model and a Lagrangian discrete bubble model. In this solver, the pure liquid and vapour phases are assumed to be incompressible and isothermal, and the pressure and velocity equations are coupled using a pressure based algorithm. The mixture properties are obtained using a linear function of liquid (or vapour) volume fraction, based on the homogenous flow assumption. Also, the liquid volume fraction is obtained by solving the transport equation model (Eulerian modelling) or from individual bubble distribution (Lagrangian modelling). In the current chapter, two Eulerian and a Lagrangian models are discribed first. Then, the coupling of the Lagrangian model with one of the Eulerian ones in the hybrid solver is explained which is followed by introducing necessary improvements to make the Eulerian-Lagrangian transition process more realizable. The described Eulerian models are the incompressible transport equation based model which is implemented in the hybrid solver and also, the compressible equilibrium model which used as a more accurate model to validate the performances of the incompressible models.

All of the numerical models have been developed in OpenFOAM (Open Source Field Operation and Manipulation) [38]; for the Lagrangian and hybrid models this involves improving the interPhaseChangeFOAM solver and coupling it with a Lagrangian library, which is an improved version of an available Lagrangian model in OpenFOAM. OpenFOAM is an open source C++ package to model and simulate fluid dynamics and continuum mechanics. It is possible to adapt the code and build new functionalities, libraries, solvers, and utilities. The spatial discretization in OpenFOAM is performed using a cell centred colocated finite volume (FV) method for unstructured meshes with arbitrary cell shapes, and a multi-step scheme is used for the time derivatives. More details about this package can be found in Weller et al. [39], Jasak [40] and Rusche [41]. In this work, the OpenFOAM version 2.3.x is used.

2.1 Compressible equilibrium EoS model

In this study, the governing equations of the compressible model are the Euler equations, which include continuity, momentum, and energy equations, similar to previous studies of Sezal [42] and Koop [2]. Due to the dominance of inertia effects in the considered cases, viscous effects can be neglected. The equations are given by

$$\frac{\partial \vec{q}}{\partial t} + \frac{\partial F_i(\vec{q})}{\partial x_i} = 0, \tag{2.1}$$

where $\vec{q}$ is the vector of conserved quantities defined as

$$\vec{q} = \begin{bmatrix} \rho \\ \rho u_1 \\ \rho u_2 \\ \rho u_3 \\ \rho E \end{bmatrix}, \tag{2.2}$$

and $F_i(\vec{q})$ is the physical flux in coordinate direction x_i, given by

$$F_i(\vec{q}) = \rho u_i \begin{bmatrix} 1 \\ u_1 \\ u_2 \\ u_3 \\ E \end{bmatrix} + p \begin{bmatrix} 0 \\ \delta_{1i} \\ \delta_{2i} \\ \delta_{3i} \\ u_i \end{bmatrix}. \tag{2.3}$$

In these equations, ρ is the mixture density and E is the specific total energy which is the sum of the specific internal energy and the specific kinetic energy. The other parameters have the same definition as before. The Euler equations are solved with the suitable temperature dependent equations of state for each phase.

In two-phase water-vapour flows, three possible states may occur: pure liquid, pure vapour, and mixture. If the calculated density is higher than the liquid saturation density, the fluid is assumed to be pure liquid. The liquid phase is then described by the modified Tait EoS [43], given by

$$p = K_0 \left[\left(\frac{\rho}{\rho_{l,sat}(T)} \right)^N - 1] \right] + p_{sat}(T), \tag{2.4}$$

where K_0 is a liquid dependent constant and $\rho_{l,sat}$ is the saturated liquid density at temperature T. Since the density of water is approximately constant, the temperature can be obtained from the caloric EoS [2, 44], which is an approximation of the complete form of internal energy equation

$$T = \frac{e - e_{l0}}{C_{vl}} + T_0, \tag{2.5}$$

where e is the internal energy of the fluid and e_{l0} is the liquid internal energy at reference temperature of T_0. Also, C_{vl} is the liquid specific heat at constant volume. When the density drops below the vapour saturation density, the fluid is assumed to be pure vapour. The perfect gas law is used to describe the pure vapour phase,

$$p = \rho R T. \tag{2.6}$$

Here, R is the specific gas constant and the temperature is obtained using the caloric EoS,

$$T = \frac{e - e_{l0} - L_v(T_0)}{C_{vv}} + T_0. \tag{2.7}$$

In this relation, $L_v(T0)$ is latent heat of vaporization at the reference temperature (T_0) and C_{vv} is the vapour specific heat at constant volume. With the thermodynamic equilibrium assumption, the mixture pressure can be considered equal to saturation pressure. Here, the temperature is calculated using the mixture internal energy as

$$T = \frac{\rho(e - e_{l0}) - \alpha_v \rho_{v,sat} L_v(T_0)}{\alpha_v \rho_{v,sat} C_{vv} + (1 - \alpha_v) \rho_{l,sat} C_{vl}} + T_0, \tag{2.8}$$

where $\rho_{v,sat}$ is the saturated vapour density at temperature T and α_v is the vapour volume fraction, computed from the mixture density as

$$\alpha_v = \frac{\rho - \rho_{l,sat}}{\rho_{l,sat} - \rho_{v,sat}}. \tag{2.9}$$

The parameters in Equations 2.4 to 2.8 are given in Table 2.1. The saturated values of pressure, p_{sat}, and liquid and vapour saturated density, $\rho_{l,sat}$ and $\rho_{v,sat}$, in the equations are obtained from IAPWS-IF97 library [45].

Table 2.1: Equilibrium model parameters

N	K_0	C_{vl} (J/kgK)	C_{vv} (J/kgK)	T_0 (K)	e_{l0} (J/kg)	R (J/kgK)	$L_v(T_0)$ (J/kgK)
7.15	3.3×10^8	4180	1410.8	273	617	461.6	2.753×10^6

In this model, the compressibility of both liquid and vapour phases is taken into account, which makes it capable of capturing possible shock waves and pressure pulses in a cavitating flow. The model has been implemented as a density-based solver in OpenFOAM by Arabnejad [46] and is similar to another earlier implemented solver [47]. The numerical flux is evaluated by solving the approximate Riemann problem using HLLC-AUSM low-Mach Riemann solver [2]. Second order accuracy in space is achieved by piece-wise linear reconstruction with the limiter function of Venkatakrishnan [48]. The solution is advanced in time using a second order explicit low storage Runge-Kutta scheme.

2.2 Incompressible finite mass transfer model

In this model, the vapour and liquid phases are treated as a single mixture fluid and mass and linear momentum are conserved in the flow domain. Here, the flow is considered as incompressible and isothermal, motivated by the balance of computational cost and model accuracy for the intended applications as described above, but a similar framework can be developed for compressible flows. Therefore, the governing equations in this model are the continuity and Navier-Stokes equations, as well as a scalar transport equation to track the liquid-vapour interface.

2.2.1 Mass and momentum conservation

Although the pure liquid and pure vapour are considered as incompressible, the mixture density varies based on volume fraction of the immiscible phases and hence the continuity equation is written by

$$\frac{\partial \rho_m}{\partial t} + \frac{\partial (\rho_m u_i)}{\partial x_i} = 0, \tag{2.10}$$

where u_i is the flow velocity vector and ρ_m denotes the mixture density, and the Navier-Stokes equation is given by

$$\frac{\partial \left(\rho_m u_i \right)}{\partial t} + \frac{\partial \left(\rho_m u_i u_j \right)}{\partial x_j} = \frac{\partial \tau_{ij}}{\partial x_j} + \rho_m g_i. \tag{2.11}$$

In this equation, g_i is the gravity vector and τ_{ij} is the stress tensor which is defined as

$$\tau_{ij} = -p \, \delta_{ij} + \mu_m \left(\frac{\partial u_i}{\partial x_j} + \frac{\partial u_i}{\partial x_j} - \frac{2}{3} \frac{\partial u_k}{\partial x_k} \delta_{ij} \right), \tag{2.12}$$

where p is the static pressure, δ_{ij} is the kronoker delta, and μ_m is the mixture dynamic viscosity. Assuming homogeneous flow, the mixture density and viscosity are obtained using the linear relations as

$$\rho_m = \alpha \rho_l + (1 - \alpha) \rho_v, \tag{2.13}$$

$$\mu_m = \alpha \mu_l + (1 - \alpha) \mu_v. \tag{2.14}$$

In the above relations ρ_l is the liquid density and ρ_v is the vapour density, while μ_l and μ_v denote liquid and vapour dynamic viscosities, respectively. α is the liquid volume fraction that specifies the relative amount of liquid in a control volume. In the utilized finite mass transfer model, the liquid-vapour interface is represented by solving a scalar transport equation for liquid volume fraction.

2.2.2 Mass transfer modelling

The liquid volume fraction transport equation is given by

$$\frac{\partial \alpha}{\partial t} + \frac{\partial (\alpha u_i)}{\partial x_i} = \frac{\dot{m}}{\rho_l}, \tag{2.15}$$

where $\dot{m}$ is the rate of mass transfer between phases. Using Equations 2.13 and 2.15, the continuity equation (2.10) may be rewritten as

$$\frac{\partial u_i}{\partial x_i} = \left(\frac{1}{\rho_l} - \frac{1}{\rho_v}\right)\dot{m}. \tag{2.16}$$

The RHS term denotes the effect of vaporization and condensation. For incompressible pressure-based solvers it is more convenient to use this form of the continuity equation, rather than Equation 2.10. Therefore, the main governing equations in this model are Equations 2.11, 2.15 and 2.16. However, to close the above set of equations, the mass transfer rate, $\dot{m}$, should also be determined. There are many numerical models proposed in literature to estimate this term and most of them are based on a simplified form of the Rayleigh-Plesset equation (later given in Equation 2.30) in which the second order derivative term as well as dissolved gas pressure, surface tension and viscous forces are neglected. The Schnerr-Sauer model [11, 38] has been used quite often in literature (e.g. [49]) and has proven to give reasonably satisfactory results for a range of applications. This model is used in the current study, but the methodology for the later explained hybrid solver does not rely on this particular choice of mass transfer model.

The Schnerr-Sauer model assumes that there are several vapour bubbles, also called nuclei, inside the liquid which act as the initial sources of cavitation inception. The number, size and distribution of these bubbles can be determined in water quality experiment tests. To simplify the numerical modelling, it is assumed that the initial nuclei have been distributed evenly throughout the liquid, and they have equal size which is the smallest size that vapour bubbles can have [50]. The vaporization and condensation rates are then given by

$$\dot{m}_c = C_c \alpha (1 - \alpha) \frac{3\rho_l \rho_v}{\rho_m R_B} \sqrt{\frac{2}{3\rho_l |p - p_{threshold}|}} \max(p - p_{threshold}, 0),$$

$$\dot{m}_v = C_v \alpha (1 + \alpha_{Nuc} - \alpha) \frac{3\rho_l \rho_v}{\rho_m R_B} \sqrt{\frac{2}{3\rho_l |p - p_{threshold}|}} \min(p - p_{threshold}, 0),$$
$$\tag{2.17}$$

where $\dot{m}_c$ and $\dot{m}_v$ are the rates of condensation and vaporization, respectively. In the above equations, R_B and α_{Nuc} are the generic radius and volume fraction of bubble nuclei in the liquid which are obtained from

$$\alpha_{Nuc} = \frac{Vol_{Nuc}}{1 + Vol_{Nuc}} = \frac{\frac{\pi n_0 d_{Nuc}^3}{6}}{1 + \frac{\pi n_0 d_{Nuc}^3}{6}}, \tag{2.18}$$

$$R_B = \sqrt[3]{\frac{3}{4\pi n_0} \frac{1 + \alpha_{Nuc} - \alpha}{\alpha}}, \tag{2.19}$$

where Vol_{Nuc} is the nuclei volume, and n_0 and d_{Nuc} are user defined parameters corresponding to the number of nuclei per cubic meter and the nucleation site diameter, respectively. Also, C_c and C_v are the condensation and vaporization rate coefficients in OpenFOAM ([38]), and $p_{threshold}$ is a threshold pressure at which the phase change is assumed to happen, usually considered as the vapour pressure of the fluid. As the overall combination of these values only influences the mass transfer rate as a constant coefficient, in this study only the vaporization and condensation rate coefficients (C_v and C_c) are modified and the fluid properties as well as model parameters are kept constant. The number of nuclei per cubic meter (n_0) is assumed to be 10^8 and the nucleation site diameter (d_{Nuc}) is set to $10^{-4} m$. Also, the liquid-vapour saturation pressure is assumed to be 2320 Pa.

To apply the finite mass transfer model in simulations, an in-house modified version of the interPhaseChangeFOAM solver is used in this study. Inter-PhaseChangeFoam is a solver for two incompressible, isothermal, immiscible fluids with phase-change (i.e. cavitation) which uses a volume fraction based approach. The set of phase-change models provided are designed to simulate cavitation but other mechanisms of phase-change are supported within this solver framework. In the in-house modified version [50, 51], the MULES corrections are omitted in the solution algorithm. More details about this solver as well as the specific implementations of the condensation and vaporization source terms of the Schnerr-Sauer model in the continuity and liquid volume fraction equations can be found in [50] and [51].

In the finite mass transfer solver, the pressure and velocity equations are coupled using a PIMPLE algorithm. This algorithm is a merge of the SIMPLE ([52]) and PISO algorithms. There are different ways to merge these algortihms, see e.g. [53]. Here, the PISO loop is complemented by an outer iteration loop, and for each time step, in every outer simple loop a special number of inner PISO loops are performed. More details about the utilized solution algorithm may be found in [54]. In the simulated flow fields, that will be discussed in the following chapter, a first order implicit time scheme is used for time discretization, the momentum equation convection terms are discretized using Gaussian linear upwind differencing scheme while the convective terms of the volume fraction scalar equation is discretized by Gaussian TVD schemes with the van Leer limiter.

One feature of the finite mass transfer approach, similar to the equilibrium EoS method, is that it treats the structures as a homogeneous mixture, therefore sparse vapour clouds or sub-grid inhomogeneity in cavitation clouds are not well treated. An extremely high mesh resolution would be required to resolve the small individual cavitation bubbles, which is not feasible in engineering applications. In addition, during the last steps of the cavity collapse and early stages of its rebound, the cavity size changes very rapidly and the bubble inertia becomes more important. However, in the simplified mass transfer model the bubble inertia, corresponding to second order derivative term in the Rayleigh-Plesset equation,

is ignored and this approach cannot fully resolve cavity collapse and rebound. The Lagrangian model, however, is potentially able to take into account the cavity inertia and is less dependant on grid resolution.

2.3 Discrete bubble model

In this model the cavities are treated as discrete Lagrangian bubbles in an ambient Eulerian continuous flow. At each time step, the Eulerian equations are solved first, then the bubbles are tracked by solving a set of ordinary differential equations along the bubble trajectory, after which the Eulerian vapour fraction is updated based on the new bubble positions and radii. The Eulerian governing equations are the continuity and Navier-Stokes equations as described for the finite mass transfer model (Equations 2.16 and 2.11).

2.3.1 Bubble equations of motion

The Lagrangian equations for tracing individual bubbles are given by

$$\frac{dx_{b,i}}{dt} = u_{b,i},$$
$$m_b \frac{du_{b,i}}{dt} = F_d + F_l + F_a + F_p + F_b + F_g, \tag{2.20}$$

where $x_{b,i}$ and $u_{b,i}$ denote the bubble position and velocity vectors, and m_b is the mass of the bubble. The RHS of the second equation includes various force components exerted on the bubbles in the $i-th$ direction, which are, from left to right, sphere drag force [55], Saffman-Mei lift force [56], added mass, pressure gradient force, buoyancy force, and gravity. These forces are given as

$$F_d = \frac{3}{4} C_D \rho \frac{m_b}{\rho_b d_b} \left(u_i - u_{b,i} \right) |u_i - u_{b,i}|,$$

$$F_l = 1.615 C_{ld} (\rho \mu)^{\frac{1}{2}} d_b^{\,2} (u_i - u_{b,i}) |\nabla \times U|^{\frac{1}{2}},$$

$$F_a = \frac{1}{2} \rho \frac{m_b}{\rho_b} \left(\frac{Du_i}{Dt} - \frac{du_{b,i}}{dt} \right)$$

$$F_p = \frac{m_b}{\rho_b} \frac{\partial p}{\partial x_i}, \tag{2.21}$$

$$F_b = -m_b \frac{\rho}{\rho_b} g_i,$$

$$F_g = m_b g_i.$$

In these relations, ρ_b and d_b are the bubble density and diameter and ρ in the density of the surrounding fluid. Also, C_D is the drag coefficient which is given by

$$C_D = \begin{cases} 0.424Re_b & Re_b > 1000 \\ 24\left(1 + \frac{1}{6}Re_b^{\frac{2}{3}}\right) & Re_b < 1000 \end{cases} \qquad (2.22)$$

where, Re_b is the bubble Reynolds number, defined as

$$Re_b = \frac{\rho d_b |u_i - u_{b,i}|}{\mu}. \qquad (2.23)$$

Also, in the lift force, C_{ld} is given by

$$C_{ld} = \begin{cases} \left(1 - 0.3314\sqrt{\frac{0.5Re_w}{Re}}\right)e^{-0.1Re} + 0.3314\sqrt{\frac{0.5Re_w}{Re}} & Re_b < 40 \\ 0.0524\sqrt{0.5Re_wRe} & Re_b > 40 \end{cases} \qquad (2.24)$$

and Re_w is the vorticity Reynolds number, defined as

$$Re_w = \frac{\rho d_b^2 |\nabla \times U|}{\mu}. \qquad (2.25)$$

Explicit implementation of flow forces is an advantage of the Lagrangian model which gives the opportunity to consider different flow effects on cavity behaviour, but it also means that the representation is dependent on the accuracy of available models for these effects. The forces typically depend on the bubble size.

2.3.2 Bubble dynamics

To find the bubble size variation due to surrounding flow, consider a spherical vapour bubble with radius R in an incompressible Newtonian fluid, Figure 2.1. Neglecting the mass transfer through the interface, the liquid velocity is equal to the interface velocity, $u(R,t) = \dot{R}$. It is assumed that the bubble is composed of vapour and dissolved gasses. Considering the balance of normal stresses at the bubble interface and ignoring the gravity effect, the pressure on the interface is given by [1]

$$p_R = p_v + p_{g0}\left(\frac{R_0}{R}\right)^{3\gamma} - 2\frac{\sigma}{R} + 2\mu\frac{\partial u}{\partial r}|_{r=R}. \qquad (2.26)$$

In this relation, p_v is the vapour pressure. The second term is the dissolved gas pressure in which p_{g0} and R_0 are the initial gas pressure and radius, while γ is the ratio of heat capacities of the gas at constant pressure and volume, i.e. c_{pg} and c_{vg}. The third term is the surface tension stress in which σ is the surface tension coefficient of the surrounding fluid, and the last term denotes the viscous stress on the bubble surface in which μ is the dynamic viscosity of the surrounding fluid and
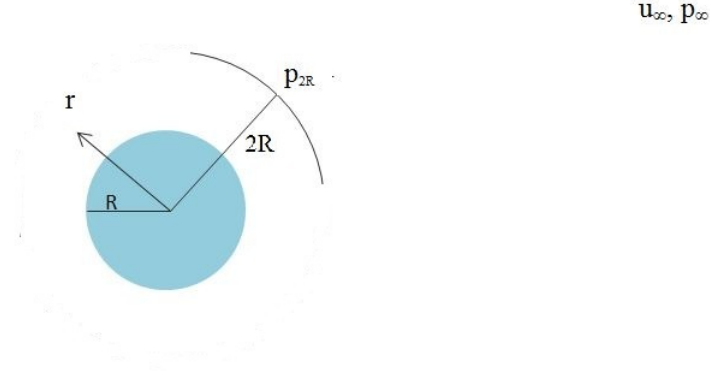
Figure 2.1: Single bubble in infinite domain

r denotes the radial component of the spherical coordinate system. In addition to the mentioned simplifications, we assume spherical symmetry around the bubble. Then, the flow around the bubble is of source (or sink) type and so irrotational. Therefore, the flow continuity and momentum equations are simplified to [1]

$$u(r,t) = \dot{R}\frac{R^2}{r^2}, \tag{2.27}$$

$$\frac{\partial u}{\partial t} + u\frac{\partial u}{\partial r} = -\frac{1}{\rho}\frac{\partial p}{\partial r}. \tag{2.28}$$

Substituting Equation 2.27 into Equation 2.28 gives

$$\ddot{R}\frac{R^2}{r^2} + 2\dot{R}^2\left[\frac{R}{r^2} - \frac{R^4}{r^5}\right] = -\frac{1}{\rho}\frac{\partial p}{\partial r}. \tag{2.29}$$

This equation can simply be integrated between any two points on a radial line from bubble interface to infinity. If the interface ($r = R$) and infinity ($r = \infty$) are chosen as integration end points, then considering the relative boundary conditions at interface (Equation 2.26) and infinity ($p = p_\infty$), the well-know Rayleigh-Plesset equation is achieved as [1, 57, 58],

$$\rho\left(R\ddot{R} + \frac{3}{2}\dot{R}^2\right) = p_v - p_\infty + p_{g0}\left(\frac{R_0}{R}\right)^{3\gamma} - 4\mu\frac{\dot{R}}{R} - \frac{2\sigma}{R}, \tag{2.30}$$

where p_∞ denotes the pressure at infinity. An inherent assumption in this equation is that the bubble is located in a completely unbounded spherically symmetric infinite domain. However, in most real case applications this assumption will not hold, as the bubble is surrounded by other cavity structures or may be confined within flow boundaries. Therefore it is more useful to take the integration between the interface and another nearby point. If the second point is chosen at $r = 2R$, then we achieve a *localized* form of Rayleigh-Plesset equation as

$$\rho\left(\frac{1}{2}R\ddot{R} + \frac{17}{32}\dot{R}^2\right) = p_v - p_{2R} + p_{g0}\left(\frac{R_0}{R}\right)^{3\gamma} - 4\mu\frac{\dot{R}}{R} - \frac{2\sigma}{R}, \tag{2.31}$$

where p_{2R} denotes the pressure at $r = 2R$. Both equations are differential and highly non-linear, due to the inertial terms. In this study, the time-step adaptive second-order Rosenbrock method is implemented to solve the Rayleigh-Plesset equation numerically (see e.g. [59] for a description of this approach). In the solution algorithm, all of the equation parameters should be specified. The surrounding fluid properties (σ, μ, γ and ρ) are constant values or may be obtained as explained before. Also, the vapour pressure, p_v, is considered as the liquid-vapour saturation pressure at the flow temperature. Then, the only unknown term is the dissolved gas pressure which is a function of the initial (or reference) radius, R_0, and gas pressure, p_{g0}, of the bubble. These parameters should be specified when a bubble is injected. For the Lagrangian solver, where new cavity structures are introduced as (parcels of) bubbles, at the injection time the bubble may be assumed to be in equilibrium with the surrounding liquid and the initial parameters can be obtained from equilibrium relations. Also, R_0 and p_{g0} can be obtained from experimental data if water quality and dissolved gas pressure are well specified. If a new bubble replaces a small Eulerian cavity (as will be explained for the hybrid solver), then the reference radius and gas pressure should be obtained from the properties of the old Eulerian cavity to avoid any unphysical transition or numerical instability.

Since the dispersed (bubble) phase in the cavitating flow is locally dense, and have properties quite different from liquid properties, the bubbles have considerable effect on the ambient flow field (similar to Eulerian cavities) as well as other bubbles. Thus, both the bubble-bubble and bubble-flow interactions should be considered in the model.

2.3.3 Bubble-bubble interaction

In the current study, the bubble-bubble interaction is considered through implementation of bubble-bubble collision. To find the collision possibility between each bubble and other bubbles, one way is to loop over all of the other bubble, and examine their positions and velocities relative to the specified bubble; however, this is a computationally expensive algorithm for dense disperse flows as the number of particles (bubbles) can be quite large. As a more effective method, in this study, the bubble-bubble collision is detected in a faster algorithm based on the "cell occupancies", Figure 2.2. The cell occupancy is a property of the grid cells which contains a label list of the bubbles that occupy a cell. Using the cell occupancy, it is possible to examine only the bubbles that are in reachable distance. Here, we need to define an interaction distance and the cell occupancies of the grid cells are transformed between every couple of cells which are within the interaction distance to each other. Consider the red bubble in Figure 2.2, for example. The interaction area is specified by a dashed circle line. Having the bubble's host cell index and the cell occupancies of the other cells in the interaction distance (i.e. within the circle) we can find the index of other bubbles that are in reachable distance. Then, the collision possibility between this red bubble and the

surrounding blue bubbles is examined. Using the cell occupancy property, it is possible to detect the collisions between the bubbles that are located at two sides of a processor boundary, in parallel computation, while in the previous approach it was not possible to send Lagrangian bubble information to a neighbouring processor. In the developed solver, the interaction distance is a user-defined parameter that can be tuned differently in different simulations.
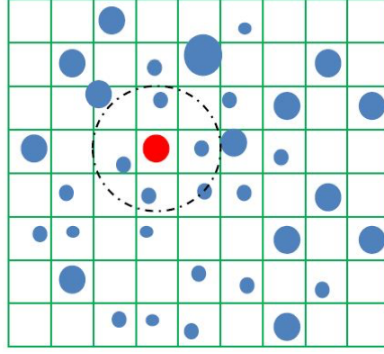
Figure 2.2: Bubble-bubble collision detection based on cell occupancy

After a collision, a pair of bubbles may coalesce to form a larger bubble or they may bounce back from each other and this is specified based on the bubbles relative velocity and the interaction time. It is known that there is a limited time available for bubble-bubble interactions, and when two bubbles approach each other, a liquid film is trapped between them which tends to resist any further movement that could bring the bubbles closer [60]. If the interaction time is long enough that the liquid film can drain to a sufficiently small thickness and rupture, the bubbles may coalesce, otherwise they bounce back from each other. The outcome of collision is therefore assumed to be a function of two time-scales, the bubble interaction time, t_i, and the liquid film drainage time, t_d. According to Chester and Hofman [61], these time scales are given by

$$
\begin{aligned}
t_i &= \left(\frac{\rho_l D_{eq}^3}{16\sigma} \right)^{1/2}, \\
t_d &= \frac{\rho_l V_{rel} D_{eq}^2}{8\sigma},
\end{aligned}
\tag{2.32}
$$

where, V_{rel} is the relative velocity between the two bubbles, and $D_{eq} = \frac{4D_1 D_2}{(D_1 + D_2)}$ is the equivalent diameter of the bubbles with diameters D_1 and D_2. The coalescence probability is expressed as

$$
P_c = e^{-t_d/t_i} = e^{-\sqrt{We/2}},
\tag{2.33}
$$

where, $We = \frac{\rho_l V_{rel}^2 D_{eq}}{2\sigma}$ is the liquid Weber number based on the equivalent diameter. If a uniform random number in the range [0,1] becomes smaller than the coalescence probability, then coalescence occurs, otherwise bouncing happens.

2.3.4   Bubble effect on the Eulerian flow field

The bubble-flow interaction can be implemented in the Eulerian equations in different ways that in large define the characteristics of the hybrid model. There are generally two methods that are used to implement the bubble effect on the Eulerian flow field. One approach is to consider the bubbles as a separate phase by defining a new void fraction for them and apply the bubble effect through correct implementation of this parameter in the Eulerian equations (Equations 2.16, 2.11 and 2.15). Also, the bubble reacting force should be applied directly as a source term in the Navier-Stokes equation. This approach is used by, e.g., Ström et al. [32]. A simpler approach, however, is to implement the bubble effect by implementing its volume fraction contribution in the calculation of mixture properties and phase change rate (Equations 2.13, 2.14 and 2.17). In this latter approach, the continuous flow is considered as a single fluid mixture, and the Eulerian governing equations are similar to the finite mass transfer model. However, the liquid volume fraction of each cell is obtained from bubble cell occupancy, instead of solving the scalar transport equation (2.15). The bubble cell occupancy for a cell is obtained based on the relative volume of the cell that is occupied by the bubble(s). This calculation includes a loop over all bubbles inside the cell and summing up the volume of these bubbles and dividing the total volume by the cell volume. Then this relative value is used to define vapour volume fraction, $1 - \alpha$, which is used to find the mixture properties from Equations 2.13 and 2.14. Due to its simplicity, the later approach is used in this study. Hsiao et al. [33] used the same method to calculate new mixture properties. Also, the continuity equation source term is obtained using the Schnerr-Sauer model (Equation 2.17). It is possible to calculate the phase change source term from bubble size and distribution variation directly, however as the main intention is to use the Lagrangian approach coupled to a FMT model to have a hybrid Eulerian-Lagrangian solver, the continuity equation is solved in a similar way to the previous method. It also helps to have a smooth transition from Eulerian cavities to Lagrangian bubbles as will be described later. It is important to note that the Lagrangian bubbles do not constitute a second phase, but they contribute as vapour structures in the mixture fluid; therefore, there is no inter-phase momentum transfer term to be considered in the Navier-Stokes equations. The implementation of the bubble effect on the Eulerian flow field is another contribution of this study which is explained in more detail in a following section for the hybrid model.

2.3.5   Bubble-wall interaction

In this study, the wall boundaries are considered to be rigid and it is assumed that a bubble collides the wall boundary when the distance between its centre to the nearest wall face becomes equal or less than its radius. When a spherical particle collides with the wall boundary, it may bounce from the wall, stick to the wall or slide over the wall surface. Experiments show that during bubble-wall collision a liquid film is present between the bubble and the wall [62]. Zenit and Legendre

[63] showed that the behaviour of a bubble colliding with a wall is different from that of a solid sphere, due to the liquid film and the bubble deformation. In this study, it is assumed that a bubble bounce from the wall.

The bubble velocity after collision depends on the relative direction between bubble velocity and the wall normal vector. If the tangential and normal unit vectors of the colliding wall face are denoted by t_w and n_w, then a bubble velocity before collision can be decomposed as

$$\mathbf{U}_b^0 = U_b^{0n}\mathbf{n}_w + U_b^{0t}\mathbf{t}_w. \tag{2.34}$$

Using this decomposition, the after-collision velocity is decomposed as

$$\mathbf{U}_b = -\varepsilon_w U_b^{0n}\mathbf{n}_w + (1-\mu_w)U_b^{0t}\mathbf{t}_w, \tag{2.35}$$

where, ε_w and μ_w are the coefficient of restitution and wall friction coefficient, respectively. ε_w is given by

$$\varepsilon_w = e^{-30\sqrt{Ca/St^*}}, \tag{2.36}$$

where Ca and St^* are the Capillary and modified Stokes numbers, defined as

$$
\begin{aligned}
Ca &= \frac{\mu U^{0n}}{\sigma}, \\
St^* &= \frac{2(\rho_b + 0.5\rho_l)RU^{0n}}{9\mu}.
\end{aligned}
\tag{2.37}
$$

An important issue in the tracking of Lagrangian bubbles, that should be considered in numerical modelling, is the relative sizes of bubbles and grid cells. Sometimes (e.g. when a new bubble is injected) a bubble may be large and occupy a number of cells. In OpenFOAM, when a bubble approaches a wall, the wall boundary condition is applied correctly only if the bubble size is smaller than the cell edge that is normal to the wall and if a bubble is larger than this limit, the bubble-wall collision is not detected properly. There are two approaches to solve this issue. The first method is to track the bubbles in a coarser grid. In this method, the Eulerian equations are solved in the main finer grid, then the obtained flow field data are mapped to a second coarser grid in which the cell edges (or at least the edges in the wall normal direction) are larger than all bubble radii. Then the bubbles are tracked in the coarser grid and the updated Lagrangian data are mapped to the finer grid to apply the bubble effect on the continuous flow field. The other remedy for this issue is to modify the wall boundary condition and redefine it based on the bubble radius rather than the edge size of the (host) cell. In the simulated flow fields of this study, that will be discussed later, the bubble-wall collisions happen in only one problem and in that case a second coarser grid is used to tack the bubbles. In the other problems, only one grid is used to track all cavity structures. When the flow data are mapped to a coarser grid, losing some resolved flow details is unavoidable. Therefore, it is recommended to revise

the numerical boundary conditions in OpenFOAM, rather than using a coarser grid. The related boundary condition is revised in the recent improvements of the solver, but in presented results of the current report, the two-grid approach is used.

The Lagrangian model is a four-way coupling model since both bubble-flow interactions and bubble-bubble interactions are considered. Also, the solution algorithm for the Eulerian equations and the equation discretizations for this model are exactly the same as for the finite mass transfer model. At each time step, the continuity and Navier-Stokes equations (Equations 2.16 and 2.11) are solved first and the updated pressure and velocity field are used to solve the Lagrangian transport equation (2.20), bubble dynamics (Equation 2.31) and bubble interactions with each other and with flow boundaries (as described in §2.3.3 and §2.3.5). The updated bubble size and distribution are then used to update the volume fraction values to obtain the new mixture properties for the next time step. The DBM model is implemented in OpenFOAM by adding a Lagrangian library to the interPhaseChangeFOAM solver, as a part of the current project. For this purpose, an improved version of the basic solidParticle class in OpenFOAM was used. The improvements in the class includes implementing the R-P equation for calculation of bubble diameter, solving the bubble-wall boundary condition issue, implementing the bubble-bubble interaction model, calculation of the vapour fraction using bubble cell occupancy function, adding different Lagrangian force models (described in Equation 2.32) and other corrections related to the parallelization of the solver. It should be noticed that in the new solver, the vapour fraction value is obtained from the distribution of the Lagrangian bubbles, and Equation 2.15 is not solved in the modified InterPhaseChangeFOAM solver.

While the bubble sizes in the Lagrangian model can be much smaller than the grid size, these models are computationally expensive when the number of bubbles is large. Also this approach is limited in representation of large and non-spherical vapour structures.

2.4   The multi-scale hybrid model

Considering the above mentioned capabilities and limitations of the Eulerian and Lagrangian formulations, the Eulerian approach is more capable in resolving large cavity structures, while the Lagrangian method is a more appropriate option for the sub-grid bubbles, and neither of the models is suitable for resolving all cavities of different length scales with reasonable computational expenses. Therefore, a hybrid Eulerian mixture - Lagrangian bubble model is developed in this study. In the hybrid model the governing equations of the continuous flow field are similar to the previous models (i.e. Equations 2.11 - 2.17) and the main difference is in the tracking of the cavity structures. Here, the cavities are categorized as Eulerian structures or Lagrangian bubbles. Then the Lagrangian bubbles are tracked using the discrete bubble method while the Eulerian structures are treated by solving the volume fraction scalar transport equation. The implementation of this model is similar to the implementation of the DBM model in OpenFOAM, however,

Equation 2.15 is not omitted from the solution algorithm, as it is solved to track the Eulerian structures. Also, an algorithm should be defined for transformation of Eulerian cavities to Lagrangian bubbles and vice versa. These implementations are performed as a part of the current research.

The categorization of the structures into Lagrangian or Eulerian groups is done based on the relative size of each cavity with respect to the local grid size of the discretized domain. If a cavity is large enough to be resolved by a threshold number of computational cells, called $N_{cell,th}$, then it is tracked in the Eulerian framework, otherwise it is treated as groups (or parcels) of Lagrangian bubbles. Also, since the volume of each cavity can change during the flow, at each time step the small Eulerian cavities or large Lagrangian bubbles may be transformed from one framework to the other. This transition is compatible with the flow physics as each Eulerian cavity normally represents a cluster of bubbles.

The hybrid model is similar to the previously developed model of Vallier [35], in turn inspired by the study of Tomar et al. [29]. However, as will be explained below, the Eulerian-Lagrangian transition as well as the Eulerian flow governing equations have been improved to avoid numerical inconsistencies in the solution algorithm.

2.4.1 Eulerian-Lagrangian transition

At each time step, small Eulerian cavity structures that are not resolved by sufficient number of computational cells, are transformed to Lagrangian bubbles. Eulerian cavity structures are recognized in the flow domain by the hosting cells' liquid volume fraction which is less than 1. Thus, to remove an Eulerian structure, the corresponding liquid volume fraction of the respective cells (α) needs to be set equal to 1. This transition is shown schematically in Figure 2.3 for a simple grid. The grid cells that have Eulerian cavities are coloured blue with $\alpha < 1$. Two of the cavities are resolved only by four cells and they are replaced by Lagrangian bubbles. Also, if a bubble later becomes large enough, it is transformed back to a Eulerian structure by deleting the bubble and setting a corresponding new α value in the occupied cells. This is a common straight-forward manner that has been
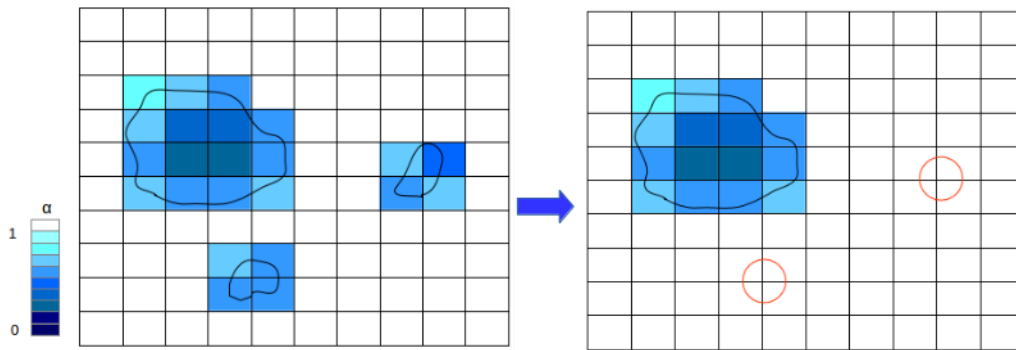

Figure 2.3: Transition of small Eulerian cavities to Lagrangian bubbles

used in earlier studies, as well. For example, in the hybrid model developed by Vallier [35], when a bubble replaces a cavity, by setting the α value to 1, it is assumed that the hosting cells are full of liquid and the bubble effect on the Eulerian field is considered as a momentum source term in the Navier-Stokes equation, similar to the contribution of a point particle. Without considering the new bubble effect in the mixture properties (as described in §2.3.4), the sudden change in the α value will cause a jump in the values of the mixture properties, ρ_m and μ_m, based on the Equations 2.13 and 2.14. Since there is a significant difference between the values of the liquid and vapour properties, this jump is considerable. Besides that, the mass transfer rate, $\dot{m}$, experiences a sudden change after removing an Eulerian vapour structure (Equation 2.17). Such significant changes in the flow properties and the continuity equation source term can cause spurious numerical pulses which may have significant unrealistic effects on the flow field. For example, these pulses can decrease the local pressure in the cavitating region which leads to generation of new vapour structures. Also, spurious pulses have negative effect on the noise prediction and erosion estimation of the flow. On the other hand, if the α value is not set to 1 after transition, then the Euler cavity is not removed and the cavity structure is modelled in both of the Eulerian and Lagrangian frameworks which causes numerical inconsistency.

Therefore, there are some issues with the current implementation of the model, including the spurious pulse problem, spurious vapour generation and insufficient consideration of bubble effect on the continuous field. A solution for these issues is presented in the following section.

2.4.2   Realizability improvement of the model

To avoid the issue described above, the coupling between the bubbles and the Eulerian mixture flow needs to be reconsidered. As mentioned before, both of the finite mass transfer and the discrete bubble models have similar governing equations in modelling the continuous flow field and the main difference is in the cavity tracking approach. Also, the vapour contribution in the mixture properties and governing equations is introduced through the α parameter. However, this parameter is not sufficient to represent both Eulerian and Lagrangian cavities at the same time. Therefore, considering $(1 - \alpha)$ to be the Eulerian vapour volume fraction in a computational cell, a new parameter is introduced to define the contribution of Lagrangian bubbles in the domain. Besides that, the continuous flow governing equations and mixture property relations should be revised to avoid spurious numerical pulses in the solution.

In order to avoid the spurious pulse problems, the mixture properties and phase change rate is defined based on a new term which is similar to α but that does not change during Eulerian-Lagrangian transition. In each bubbly cell, the cell volume is occupied by both Eulerian fluid and Lagrangian bubbles. The fluid contribution in the cell is defined by a new parameter which is called β; similarly the bubble volume fraction in the cell is $1 - \beta$. It is obvious that in cells containing

bubbles, β is less 1, while it is equal to 1 everywhere else. During the Eulerian to Lagrangian transition, a vapour structure which occupies $(1-\alpha)$ fraction of the hosting cells is replaced by a bubble which occupies $(1-\beta)$ fraction of the same cells. Therefore the new value of β in the host cells is the same as the old value of α. Also, the new value of α is 1 which is exactly the same as the old value of β since there were no bubbles in the host cells before the transition. In other words, both α and β have similar sudden changes, however their product $\alpha\beta$ does not change during the Eulerian-Lagrangian transition. In the bubble cells, where $\alpha = 1$, $\alpha\beta$ has the same value as β and everywhere else it is equal to α. Consequently, this parameter is suitable to replace α in the definition of mixture properties and calculation of phase change rate, $\dot{m}$. Therefore, the mixture properties formula can be modified as

$$\begin{aligned}
\rho_m &= \alpha\beta\rho_l + (1-\alpha\beta)\rho_v, \\
\mu_m &= \alpha\beta\mu_l + (1-\alpha\beta)\mu_v.
\end{aligned} \tag{2.38}$$

Further, the phase change rate formula is modified as

$$\dot{m}_c = C_c\alpha\beta(1-\alpha\beta)\frac{3\rho_l\rho_v}{\rho_m R_B}\sqrt{\frac{2}{3\rho_l|p-p_{threshold}|}}\max(p-p_{threshold},0),$$

$$\dot{m}_v = C_v\alpha\beta(1+\alpha_{Nuc}-\alpha\beta)\frac{3\rho_l\rho_v}{\rho_m R_B}\sqrt{\frac{2}{3\rho_l|p-p_{threshold}|}}\min(p-p_{threshold},0).$$
$$\tag{2.39}$$

Using the above equations avoids drastic changes and large spurious pulses in the flow. Therefore, a new parameter, β, is defined to consider the Lagrangian cavities contribution and the governing equations are reformulated based on the $\alpha\beta$ parameter.

However, two minor corrections are still needed in the multi-scale solver. During the transition, in each cell of the host cells group, the new value of β should be exactly equal to the old value of α to keep the $\alpha\beta$ parameter conserved. In other words, the bubble contribution in each cell should be equal to the contribution of the corresponding Eulerian cavity. However, while the summation of cavity contribution (old α) is the same as the summation of bubble contribution (new β), their individual contribution in each single cell is not equal since they have different geometrical shapes (Figure 2.3). As a solution, instead of injecting one large bubble, the vapour structure is replaced by a group of small bubbles which do not occupy more than 1 cell. The size of new bubbles in each cell are determined based on the old value of α such that the value of $\alpha\beta$ is conserved in that cell. The improved transition approach is shown schematically in Figure 2.4. The blue cells include Eulerian cavities and the red ones are occupied by Lagrangian bubbles. In the white cells both α and β are equal to 1. Also, instead of large bubbles, several smaller bubbles are injected, as compared to Figure 2.3. This leads to an increase in computational cost, as more bubbles are introduced, but gives a significantly improved representation of the smaller vapour structures. It

is important to note that the vapour volume fraction of the small Eulerian cavities are less than one, which means that the cavity is not pure vapour. In other words, during Eulerian-Lagrangian transition we are dealing with a small cloud of many bubbles (distributed in the surrounding liquid) and not a single bubble full of pure vapour. From the Eulerian data it is not possible to obtain the distribution of bubble diameters and positions in this small cloud. However, it is interesting to know that the bubble distribution and sizes do not considerably change the collapse rate of the total cloud from an Eulerian point of view and this point can be inferred from the works of Schmidt et al. ([3] and [36]). In these studies, a group of bubbles with *nonuniform distribution* in position and size were simulated both as individual bubbles as well as an equivalent cloud and the results show that both simulations lead to quite similar collapse profile. Therefore, replacing the cavity with more smaller bubbles rather than one single large bubble, not only solve the numerical pulse issue, but also makes the transition more aligned with real physics. The small bubbles can have different distributions in size and position, however, to decrease the computational expenses it is suggested to keep the number of bubbles as low as possible, therefore only one or two bubbles are injected in each cell as in Figure 2.4.
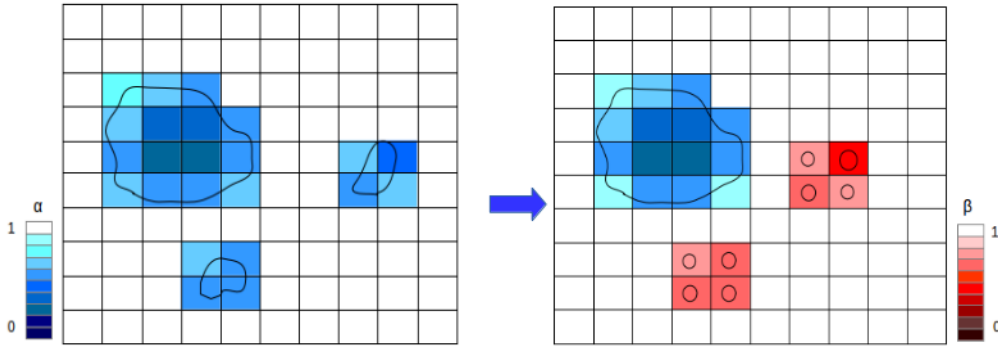
Figure 2.4: Improved transition; the blue contours show the Eulerian cavity volume fraction and the red contours depict the Lagrangian bubble contribution

Avoiding vapour generation in the bubbly cells is one further improvement needed in the solver. In each computational cell that contains vapour, the cavity structure should be tracked either by the Eulerian transport equation or the Lagrangian bubble tracking algorithm. In other words, there cannot exist an Eulerian cavity in a cell that is occupied by a Lagrangian bubble, and vice versa. To avoid compromising this situation, the mass transfer source term in the volume fraction equation should be omitted in the bubbly cells. Thus, Equation 2.15 is rewritten as

$$\frac{\partial \alpha}{\partial t} + \frac{\partial (\alpha u_i)}{\partial x_i} = \frac{\dot{m}}{\rho_l} * pos(\beta - 1). \tag{2.40}$$

When there is a bubble in a cell, β is less than 1, therefore the $pos(\beta - 1)$ equals zero and no vapour is generated in the cell. Without this modification an Eulerian

structure can be generated in bubble host cells, according to Equation 2.39, as the flow pressure is usually equal or less than the threshold (vapour) pressure in these cells. Then, the vapour structure in such cells and its contribution to the mixture properties will be considered twice. Besides that, the new Eulerian cavity is small at the time of generation and therefore it will be transformed into a Lagrangian bubble in the next time step and then the new and old bubbles can coalesce and make a larger bubble. And this process can be repeated in each time step by generating new Eulerian structures which lead to an unstable and unphysical growth of the Lagrangian bubble.

2.4.3 Solution strategy

The final solution strategy consists of two algorithms. The major algorithm to solve the flow governing equations, and another algorithm for Eulerian-Lagrangian transition. In the developed solver, after initializing of the flow field and defining the solution parameters, in each time step the governing equations are solved in the following order:

Algorithm 1 Solution procedure

 1: **for** `t=start time:end time` **do**

 2:     Solve Equation 2.11 to obtain new velocity field.

 3:     Find the mass transfer rate, $\dot{m}$, from Equation 2.39.

 4:     Obtain the new pressure field, by solving Equation 2.16.

 5:     Update the mass transfer rate, $\dot{m}$, from Equation 2.39.

 6:     Solve Equation 2.40 to find the new liquid volume fraction field.

 7:     Solve Equations 2.20 and 2.30 for each bubble to obtain the new positions and diameters.

 8:     Perform the mixture-bubble transition algorithm (algorithm 2).

 9:     Update the mixture properties by solving Equation 2.38.

10: **end for**

The second algorithm is the Eulerian mixture - Lagrangian bubble transition algorithm. The original step-by-step transition process is explained by Vallier [35]. However, to meet the currently introduced improvements, the algorithm needs to be revised. Similar to Vallier's approach, in the first step all of the cavity structures in the flow domain are detected. Next, the number of computational cells that represent each structure are counted. If this number is less than a threshold value (e.g. 5, in this study), it is decided that the relative structure is not

represented by sufficient number of grid cells. Then, for each cavity that is not well resolved, the algorithm 2 is followed.

Also, if a Lagrangian bubble collides with a large Eulerian cavity, or it becomes large enough to be resolved by sufficient number of cells, it will be transformed to an Eulerian structure by deleting the bubble, while in the host cell β is set to 1 and $\alpha = \beta_{old}$. The transition criteria can be improved in further development of the model, which is the topic of a future study.

Algorithm 2 Transition algorithm

1: Create a list of cell labels $\{$cell j , j=1:J$\}$, associated with the cavity structure.

2: **for** j=1:J **do**

3:     Evaluate the cavity volume $V_{vapour,j}$.

4:     Find the minimum edge length of the cell, $\Delta_{min,j}$

5:     Find the minimum No. of bubble(s) in the cell, N_b, and the largest possible bubble radius, R_b, so that

    $N_b \frac{4}{3}\pi R_b{}^3 = V_{vapour,j}$,
    $R_b < \Delta_{min,j}$.

6:     **for** k=1:N_b **do**

7:         Find the bubble position vectors $\mathbf{X}_{b,k}$ in the cell j:
        The positions vectors are N_b points in the cell volume with uniform distribution.

8:         Set the bubble velocity, $\mathbf{U}_b$, equal to the Eulerian mixture velocity in the cell, $\mathbf{U}_j$.

9:         Inject the bubble

10:     **end for**

11:     Remove the Eulerian cavity of the cell by setting $\alpha_j = 1$.

12: **end for**

3

Results

In this chapter, the performances of different introduced models in simulating benchmark problems are investigated, and the implementation of the new hybrid Eulerian-Lagrangian solver is verified and validated. In the following results, first the Lagrangian model is compared with the equilibrium EoS and finite mass transfer model by studying two benchmark test cases to understand the capabilities and limitations of each method. The first case studied is the collapse of a single bubble in an infinite domain, which helps to understand each model behaviour in capturing the cavity interface and the surrounding pressure variations. The special differences between the Lagrangian and finite mass transfer models in this case clarify some possible origin for some limitations of the latter method as well. The second investigated case is the collapse of a cluster of bubbles, where the collapse of each bubble is affected by the dynamics of surrounding bubbles. This case confirms the importance of considering local pressure in the improved form of the Rayleigh-Plesset equation (2.31) and illustrates the influence of the liquid compressibility for cavity modelling and appropriate capturing of the collapse pressure pulses. Also, in a third test case, the improvements of Eulerian-Lagrangian transition algorithms (§2.4.2) is verified through a qualitative results of the 2D cavitating flow around a hydrofoil.

3.1   Single bubble collapse

The collapse of a single bubble is a benchmark test case that has been widely used for primary validation of different numerical models in literature. Here the collapse of a vapour bubble in an infinite medium with atmospheric pressure is simulated and the effects of viscosity, non-condensible gas, surface tension and gravity are ignored. This problem is also known as the Besant problem and can be solved analytically. Although the pressure at infinity has constant atmospheric value, its radial distribution from the bubble interface to the surrounding liquid is
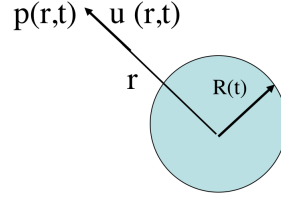
Figure 3.1: Single bubble collapse

not uniform (Figure 3.1), and it has a Laplacian distribution according to Equation 2.29.

As described by Franc and Michel [1], the collapse time of the bubble, also known as the Rayleigh time, is given by,

$$\tau_R = 0.915 R_0 \sqrt{\frac{\rho}{p_\infty - p_v}}. \qquad (3.1)$$

Further, by integrating the Rayleigh-Plesset equation, the collapse rate is obtained as,

$$\frac{dR}{dt} = -\sqrt{\frac{2}{3} \frac{p_\infty - p_v}{\rho} \left[\frac{R_0{}^3}{R^3} - 1 \right]}. \qquad (3.2)$$

From this relation, the bubble radius profile can be calculated analytically. The pressure distribution around the bubble is determined from Equation 2.29 as

$$\Pi(r) = \frac{p(r) - p_\infty}{p_\infty - p_v} = \frac{R}{3r} \left[\frac{R_0{}^3}{R^3} - 4 \right] - \frac{R^4}{3r^4} \left[\frac{R_0{}^3}{R^3} - 1 \right]. \qquad (3.3)$$

Here, we consider the case where initial bubble radius is 0.4 mm and the flow is assumed to be initially at rest. The pressure inside is $p_v = 2,320$ Pa. Also, the liquid volume fraction is set to 0.01 inside the bubble and equal to 1 outside. The mass transfer rate in the Schnerr-Sauer model is a function of $\alpha(1-\alpha)$, which means that for pure liquid and pure vapour the rate of condensation or vaporization term is zero and to start the cavitation process, the initial α value of the vapour region should be set to a very small but non-zero value (here, 0.01). In the vaporization term, we have an α_{Nuc} term as well, but it is too small to ensure a sufficient initial rate of cavitation. Considering the spherical symmetry of the flow field, only an asymmetric wedge mesh with an angle of five degrees is created (Figure 3.2a). The far field boundary is located 0.5 m from the bubble centre, with a fixed atmospheric pressure (10^5 Pa) and zero gradient conditions for liquid volume fraction and velocity. The total domain is discretized with 5,000 cells, including 100 points in the radial direction. The initial bubble is well resolved by 20 cells in the radial direction and 50 cells in the circumferential direction. The generated grid with the initial pressure field is depicted in Figure 3.2b; it is radially uniform inside the bubble. For the Lagrangian model simulation, instead of liquid volume fraction initialization, a 0.4 mm bubble is injected at the first time step and the corresponding liquid volume fraction is calculated from bubble cell occupancy. The liquid

and vapour densities are assumed to be $\rho_l = 1000\,\mathrm{kgm^{-3}}$ and $\rho_v = 0.01389\,\mathrm{kgm^{-3}}$, and the corresponding dynamic viscosity values are set as $\mu_l = 0.001\,\mathrm{kgm^{-1}s^{-1}}$ and $\mu_v = 10^{-5}\,\mathrm{kgm^{-1}s^{-1}}$. The solution time step is set to 5×10^{-9} s for incompressible simulations and 1×10^{-10} s (corresponding to CFL number of 0.32) for the equilibrium model. Therefore, for the incompressible simulations we have $\Delta t/\tau_R = 1.35 \times 10^{-4}$, and for the compressible simulation $\Delta t/\tau_R = 2.7 \times 10^{-6}$. However, larger time steps are also used for time-step dependency studies. In the following sections the results of each model when solving this problem are compared with the theoretical solution.
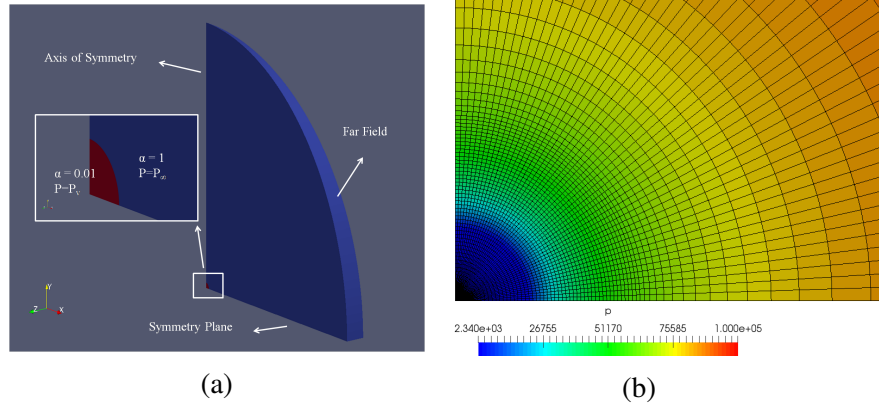

Figure 3.2: Single bubble; (a) flow domain with initial vapour fraction; (b) generated grid with initial pressure distribution

It should be mentioned that for all cases the pressure profiles are compared with the theoretical values up to 0.975 of the collapse time. At this instance, the bubble interface velocity is about 48 m/s according to Equation 3.2 ($R/R_0 \approx 0.3$), which corresponds to very low Mach numbers in liquid and therefore the liquid flow field can be considered to be incompressible and the velocity to be divergence free. Therefore, Equation 3.3 can be applied at the investigated instances and the numerical results can be compared with the theoretical solutions as long as the liquid compressibility does not have a considerable effect on the numerical methodologies.

3.1.1 Equilibrium model result

The numerical evolution of bubble radius with time is compared with the exact analytical solution in Figure 3.3. In this plot, the radius and the evolution time are non-dimensionalized by initial radius and Rayleigh collapse time, respectively. Since the bubble interface may not be perfectly sharp at all time steps, R is the equivalent radius of the total vapour volume. As depicted in the figure, the radius profile is well captured by this method.

In Figure 3.4, the pressure distribution in the radial direction is compared with the analytical data at different normalized time steps. In this figure, the normalized
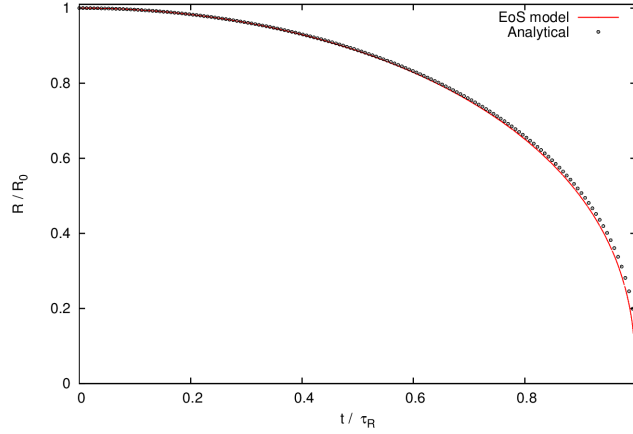
Figure 3.3: Validation of the equilibrium (EoS) model in predicting the evolution of the bubble radius

times t/τ_R of 0.812, 0.894, 0.921, 0.948 and 0.975 are chosen which are corresponding to non-dimensional radius (R/R_0) values of 0.64, 0.52, 0.47, 0.4 and 0.3, respectively. At these steps, the bubble size variation is quite fast and the surrounding flow field changes rapidly. Before $t/\tau_R = 0.812$, the pressure variations around the bubble does not have large gradients and the profile is rather similar to the initial distribution. Considering the stated assumptions, the pressure is expected to be equal to the vapour pressure inside the bubble, which corresponds to a non-dimensional value of -1. From the bubble interface to the farfield, the pressure increases to the farfield pressure. However, according to Equation 3.3, its profile has a maximum value close to the interface if $R/R_0 < 0.63$ [1]. This behaviour is clearly seen from the analytical solution in Figure 3.4. The numerical results also follow the general trend, but with some noticeable differences. First, the pressure near the interface is still close to vapour pressure and the pressure increase starting point seems to be at a radius larger than the bubble radius. Also, the pressure is underestimated outside of the bubble, especially at the later steps, i.e $t/\tau_R = 0.948$ and 0.975. Besides that, some large wiggles are seen in the pressure profile which are due to numerical pressure waves that are emitted from bubble interface. When the fluid phase changes from vapour to liquid in a computational cell, there is a change in the relative equation of the state for the fluid and the general profile of the density-pressure relation changes. Such a change in the modelling equations causes some spurious pulse in the flow. Since in the polar grid, cells are aligned with the interface and phase change occurs in all cells of a radial layer simultaneously, then numerical pulses of the neighbouring cells are superposed and generate a significant disturbance. In a cartesian grid, for example, the vapour condensation at neighbouring cells does not happen simultaneously and the wiggles in the pressure profile are expected to cancel and be smaller; this is observed in the second case of the bubble cluster. Furthermore, these pulses are a function of numerical discretization schemes as well and more diffuse schemes are expected to generate smaller pulses.
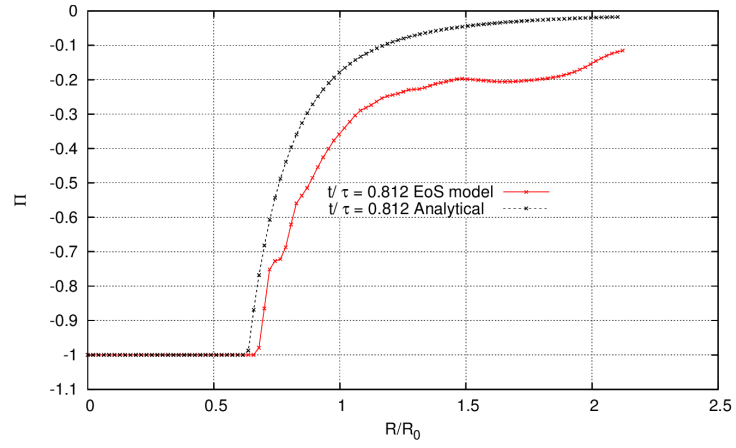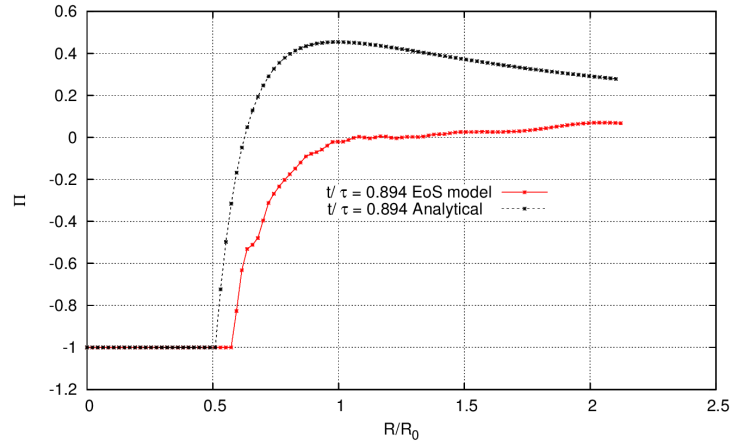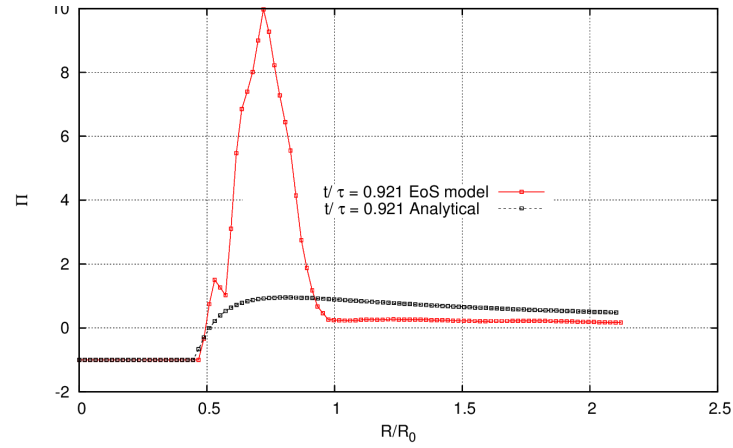
(a) t / τ_R = 0.812

(b) t / τ_R = 0.894

(c) t / τ_R = 0.921

Figure 3.4: Comparison of equilibrium (EoS) model pressure distribution with analytical data at different time steps

(d) t / τ_R = 0.948
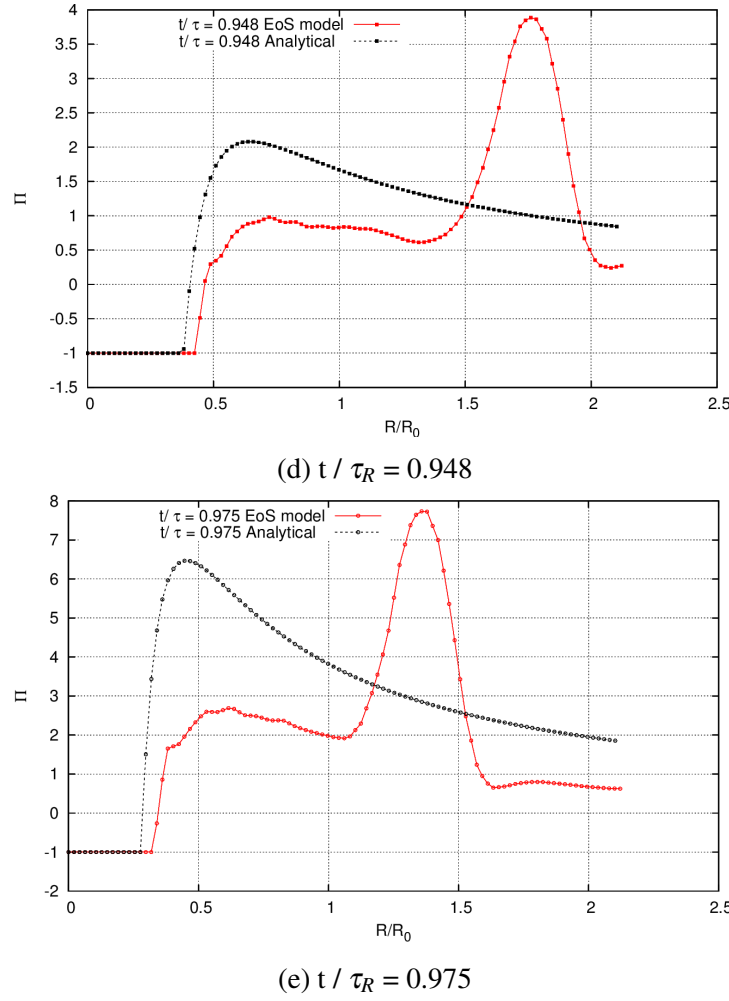

(e) t / τ_R = 0.975

Figure 3.4: Comparison of equilibrium (EoS) model pressure distribution with analytical data at different time steps (cont.)

The first inconsistency, that is the delay in the pressure increase starting point, can be due to the numerical diffusivity of the bubble interface, shown in Figure 3.5. In this figure, an imaginary red line shows the exact bubble radius overlayed on predicted vapour fraction and pressure fields at $t/\tau_R = 0.812$. In Figure 3.5a, the computed vapour fraction distribution over the discretized domain is shown. It is seen that the bubble interface is diffused over three layers of radial cells (the orange, the green and the light blue cells), which means that in these cells the fluid is considered as a saturated mixture in the equilibrium model and the pressure in the last layer (outside exact bubble radius) cannot vary considerably from vapour pressure. It should be mentioned that the maximum value of the α contour is increased to 1.05 for an easier detection of the orange layer. In Figure 3.5b, the pressure contour around the bubble is depicted. It is seen in this figure that the pressure is equal or close to the vapour pressure up to one cell layer after the bubble radius. Since the radial edge size of each cell is 0.02 mm (initial radius
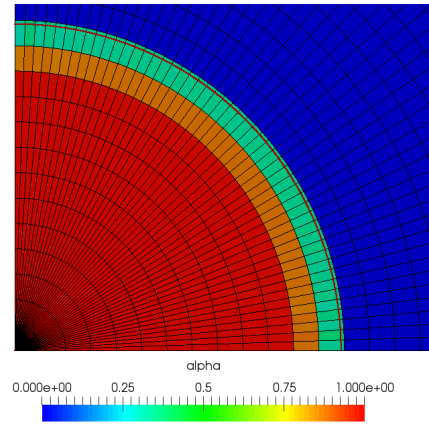
(a)
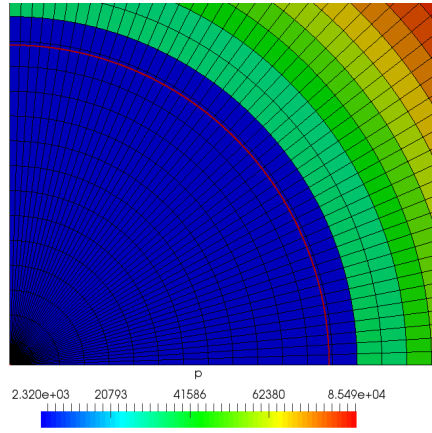
(b)
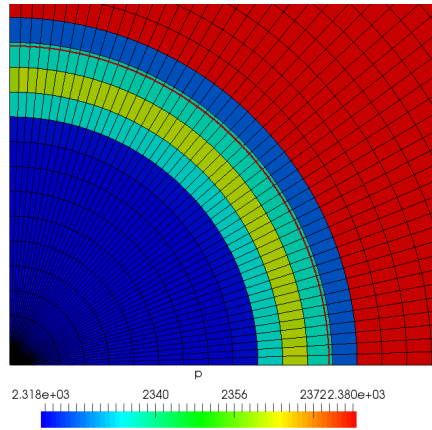
(c)

Figure 3.5: Resolution of bubble interface from the equilibrium model at $t/\tau_R = 0.812$; (a) vapour volume fraction contour; (b) pressure contour at global scale; (c) pressure contour at local scale. The red line depicts the bubble radius of the analytical solution.

is resolved by 20 radial cells) this discrepancy is comparable to what is shown in Figure 3.4. Besides, it can be seen that in the second and third radial layers after the bubble, the pressure is not uniform in the circumferential direction while it is expected to be uniform from the flow symmetry. This means that there are some numerical fluctuations in the estimated pressure field around the interface. In Figure 3.5c, the same contour is plotted with local scale (i.e. $2,320 < p < 2,380$ Pa) and it shows that inside the bubble the pressure is not exactly constant, especially in four radial layers where the fluid is saturated mixture, c.f. Figure 3.5a. In these layers, the temperature has a small variation (less than 0.5 degrees) and it causes around 40 Pa variation in the saturated pressure value. This is one of the capabilities of the temperature dependant equations of states that consider the temperature changes during cavitation.
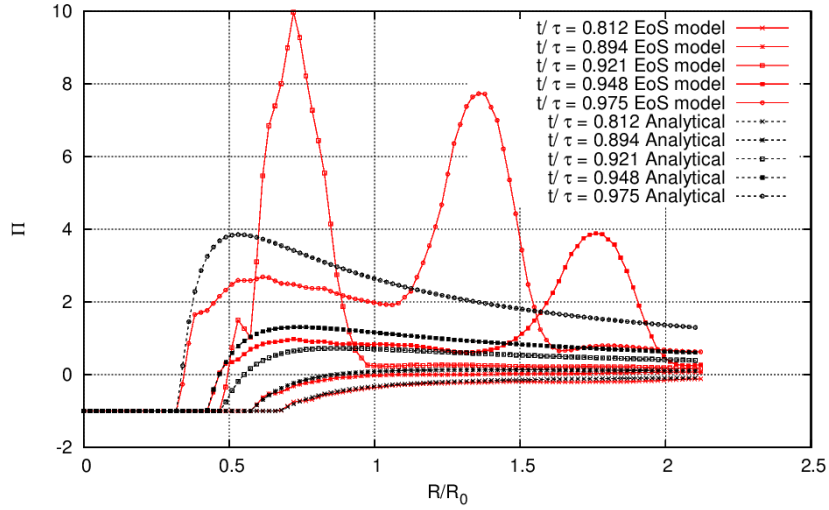

Figure 3.6: Comparison of equilibrium (EoS) model pressure distribution with analytical data with shifted interface

To have a better understanding of the model performance in calculation of pressure field outside the bubble, the analytical data are shifted a little in Figure 3.6. In fact, in the new analytical profiles, the sharp bubble interface is assumed to be equal to the outer edge of the diffused numerical interface so that both pressure profiles have similar gradient at the interface. From this figure it can be inferred that the equilibrium model would be capable to resolve outer pressure profile more reasonably if the interface could be captured sharply and at the correct location.

To investigate the effect of the grid resolution on the model results, the problem is solved with a coarser grid in which the initial bubble is discretized with 12 cells (i.e. $\Delta_r/R_0 = 0.083$). In Figure 3.7, the estimated bubble radius and pressure profiles are compared with the corresponding ones of the fine grid. For the bubble radius, the results are very similar, however, considerable differences are seen for the pressure estimation. For the coarse grid, the maximum nondimensional pressure peak is 32, which is not seen in the plot range.

(a)

(b)
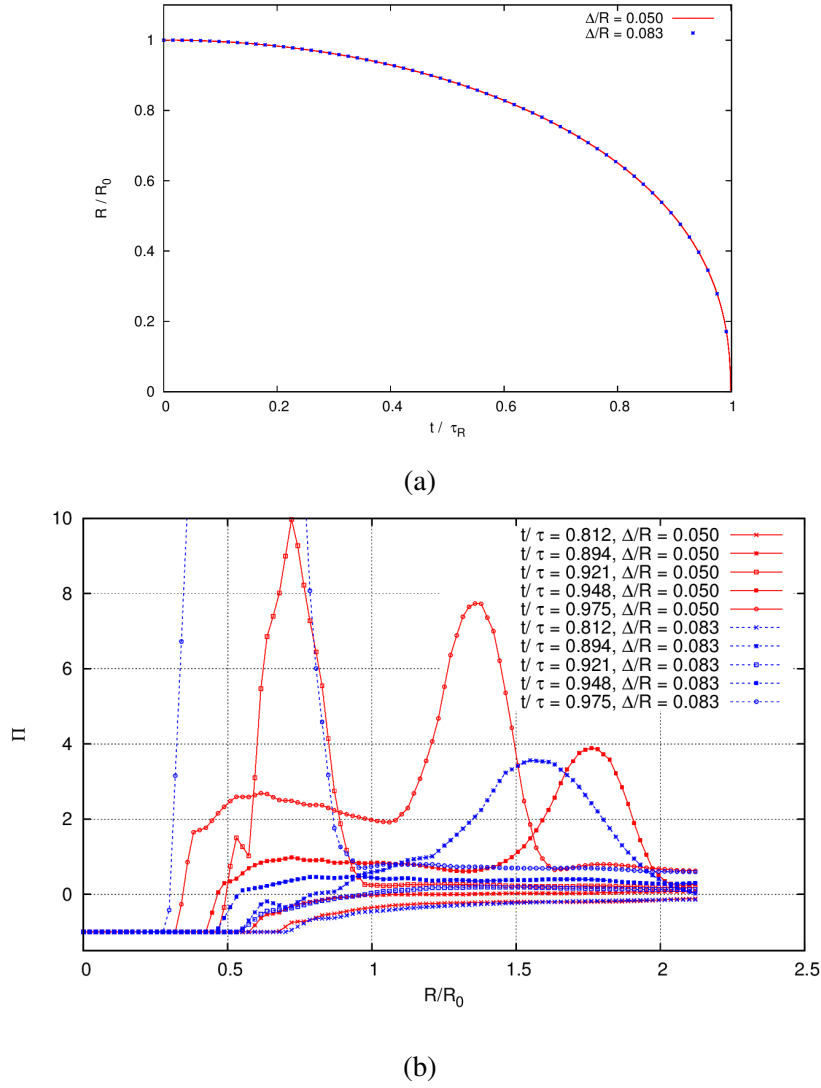
Figure 3.7: Domain discretization effect on the equilibrium model; (a) bubble radius; (b) pressure profile

Finally, it should be noted that for this special problem, the liquid compressibility effect is negligible. According to the depicted pressure profiles (e.g. Figure 3.4), up to the investigated time instances, the maximum pressure value in the domain is around 8 bar ($\Pi = 7$) while the minimum driving pressure is 1 bar. According to the Tait equation (Equation 2.4) water density variation for this range of pressure change is less than 0.1 percent and the liquid can be considered to be incompressible and Equation 3.3 is applicable.

3.1.2 Finite mass transfer model result

As mentioned in the previous chapter, for the pressure-velocity coupling of the pressure based models, the PIMPLE algorithm is used in this study. For this test

case, at each time step, one outer SIMPLE loop is performed, and in each SIMPLE loop at least three PISO loops are performed. Therefore, the solution algorithm is practically a PISO loop, using three corrector steps in each time step.

The temporal evolution of bubble radius for the finite mass transfer model is compared with the exact analytical solution in Figure 3.8. According to this figure, the finite mass transfer model is capable in estimation of bubble radius profile if the empirical coefficients are set high enough. In fact, for low rate coefficients, the bubble collapses very slowly.
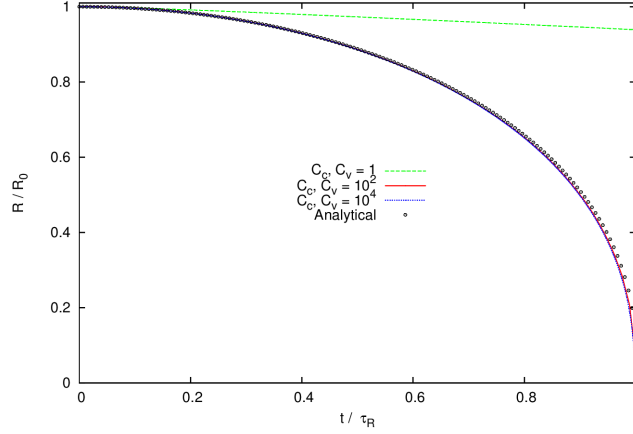

Figure 3.8: Validation of the finite mass transfer model with different coefficients in predicting the evolution of the bubble radius

To have a better understanding of the model performance for this flow, the collapse pressure profiles are compared with analytical data in Figure 3.9. It is seen that although moderate coefficient values ($C = 100$) can capture the radius evolution, there may be numerical issues in representing the pressure field. In Figure 3.9a, it is seen that in the last stages of collapse ($t/\tau_R > 0.921$), the pressure inside the bubble is overestimated. Besides that, some numerical pulses are emitted from the interface which cause the outside pressure at $t/\tau_R = 0.921$ to be higher than the corresponding value at $t/\tau_R = 0.948$, for example. Here, ignoring the pure phase compressibility is also affecting the prediction. As seen in the compressible equilibrium model results (Figure 3.4), a numerical pulse causes a pressure wave that is emitted gradually in the domain and therefore, only the local pressure is increased. However, for the finite mass transfer model in this study, the liquid is assumed to be incompressible and a local numerical pulse increases the whole domain pressure instantaneously. Therefore, the outside pressure profile at $t/\tau_R = 0.921$ is higher than the corresponding profile at $t/\tau_R = 0.948$. Further increasing the coefficient to 500 or 1000 solve the inside pressure overestimation issue, however, the numerical pulses get more significant. If the coefficients are increased to 10^4, then both of the issues are approximately addressed. However, similar to the equilibrium model, the interface is diffused and the pressure increase starting point is shifted a little in the radial direction and the pressure peaks are underestimated. If the coefficients are increased to very high values (Figure

(a)

(b)

Figure 3.9: Comparison of finite mass transfer (FMT) model pressure distribution with analytical data; (a) $C_c = C_v = 10^2$; (b) $C_c = C_v = 500$; (c) $C_c = C_v = 10^4$; (d) $C_c = C_v = 5 \times 10^6$

3.9d) the pressure profile does not change considerably. However, comparison of profiles at $t/\tau_R = 0.921$ and 0.894 shows that small numerical pulses still exist in the simulation. It should be mentioned that increasing the model constants may decrease the stability of the problem and special measures should be done to make sure a converged solution of the vapour transport equation is achieved. The general trend of pressure profile relative to the model constants are in agreement with the work of Schenke and van Terwisga [64] in which they used the Merkle mass
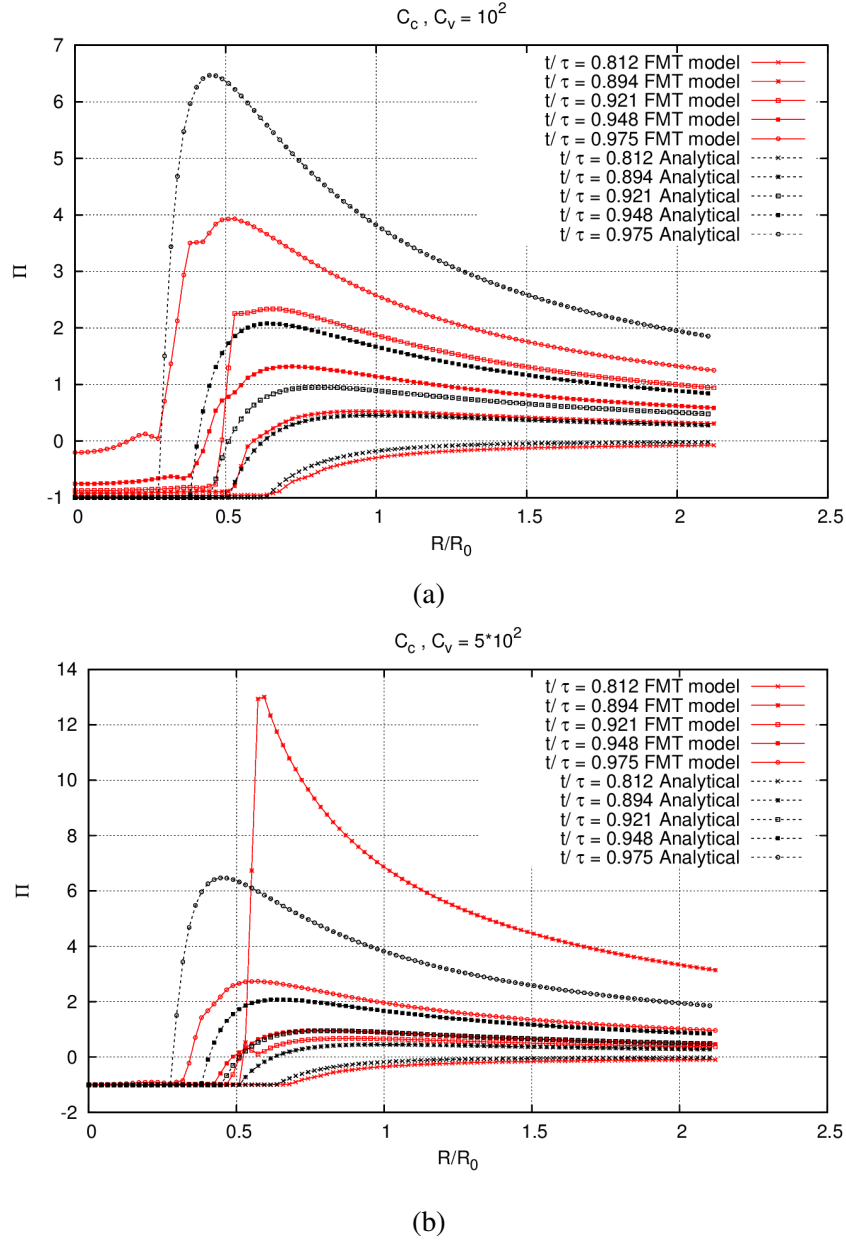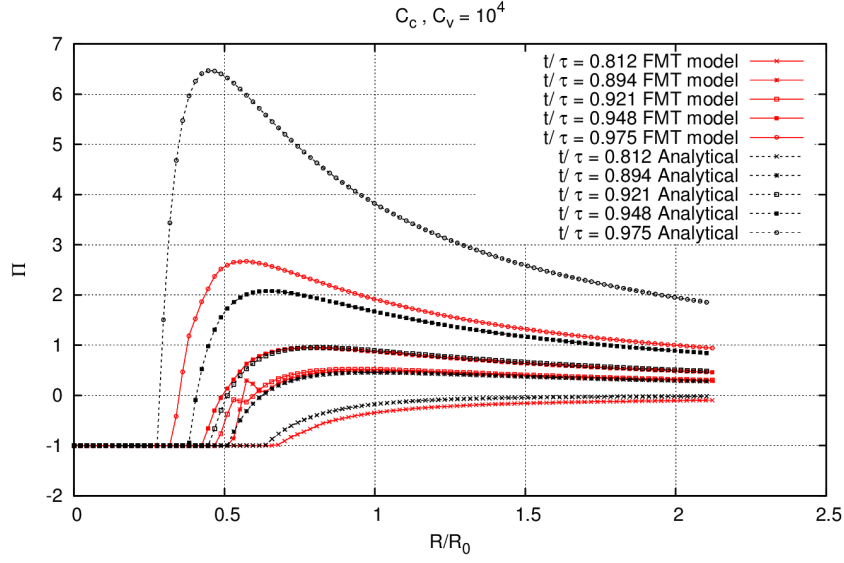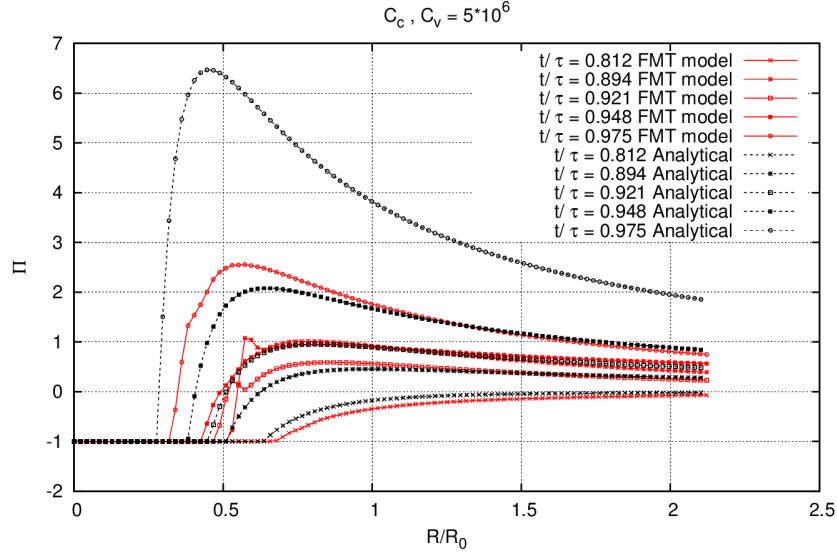
(c)

(d)

Figure 3.9: Comparison of finite mass transfer (FMT) model pressure distribution with analytical data; (a) $C_c = C_v = 10^2$; (b) $C_c = C_v = 500$; (c) $C_c = C_v = 10^4$; (d) $C_c = C_v = 5 \times 10^6$ (cont.)

transfer model [12] and concluded that for more satisfactory prediction of bubble Rayleigh collapse, the model constants should be quite large while the time steps should be fine enough.

Another parameter that can be effective on model performance is the time step size. In this study, the very small time step of 5×10^{-9}s was chosen at first, to make sure that it works for different applied models. This value may work for EoS model as well, but to avoid some pressure fluctuations and to satisfy the CFL

number limitation, a smaller time step was used in the compressible approach. For the FMT model, however, a time step study (Figure 3.10) shows that the time step should be smaller than 5×10^{-8} s to ensure time-step independent solution. Further time step study (not reported here) confirms converged solution using dt = 5×10^{-9} s. However, smaller time step may increase the solution instability, and the solution parameters need to be set more carefully, e.g. by decreasing the solution tolerances or setting a minimum number of iterations, to ensure converged result for high values of mass transfer coefficients. Also, from Figure 3.10 it seems that the spurious pulses may be avoided by increasing the simulation time step; however, it can be shown that there is not a predictable relation between these pulses and the time step, as for time steps larger than 5×10^{-8} s (e.g. 1×10^{-7} s), some spurious pulses are seen in the domain that are larger than the previous ones.

(a)

(b)
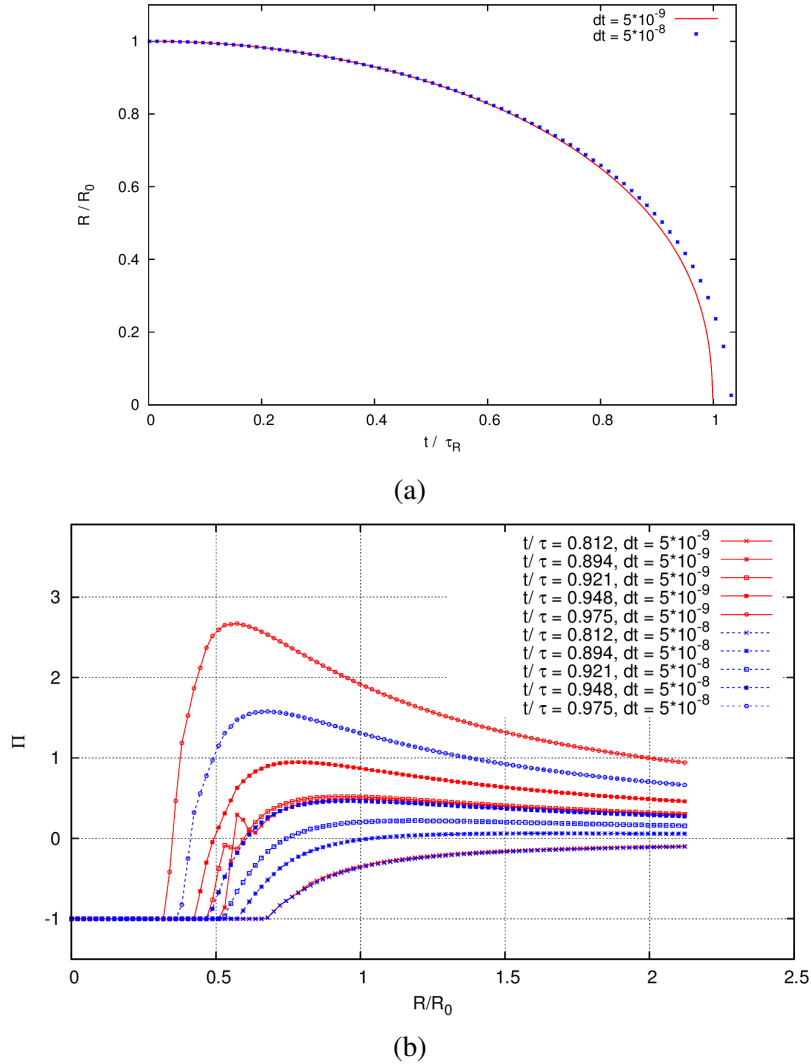
Figure 3.10: Time-step dependency of the finite mass transfer model; (a) bubble radius; (b) pressure profile

To investigate the model dependency on the grid resolution, the problem is solved with a coarser grid ($\Delta_r/R_0 = 0.083$) as well. In Figure 3.11, the estimated bubble radius and pressure profiles with empirical coefficients of 10^4 are compared with the corresponding ones of the fine grid. It is seen that while the bubble radius is well estimated with the coarser grid, considerable numerical pulses exist in the solution even with the high mass transfer coefficients. This is an important point, since in typical engineering problems, the small cavity structures are not discretized with very fine grids.

(a)

(b)

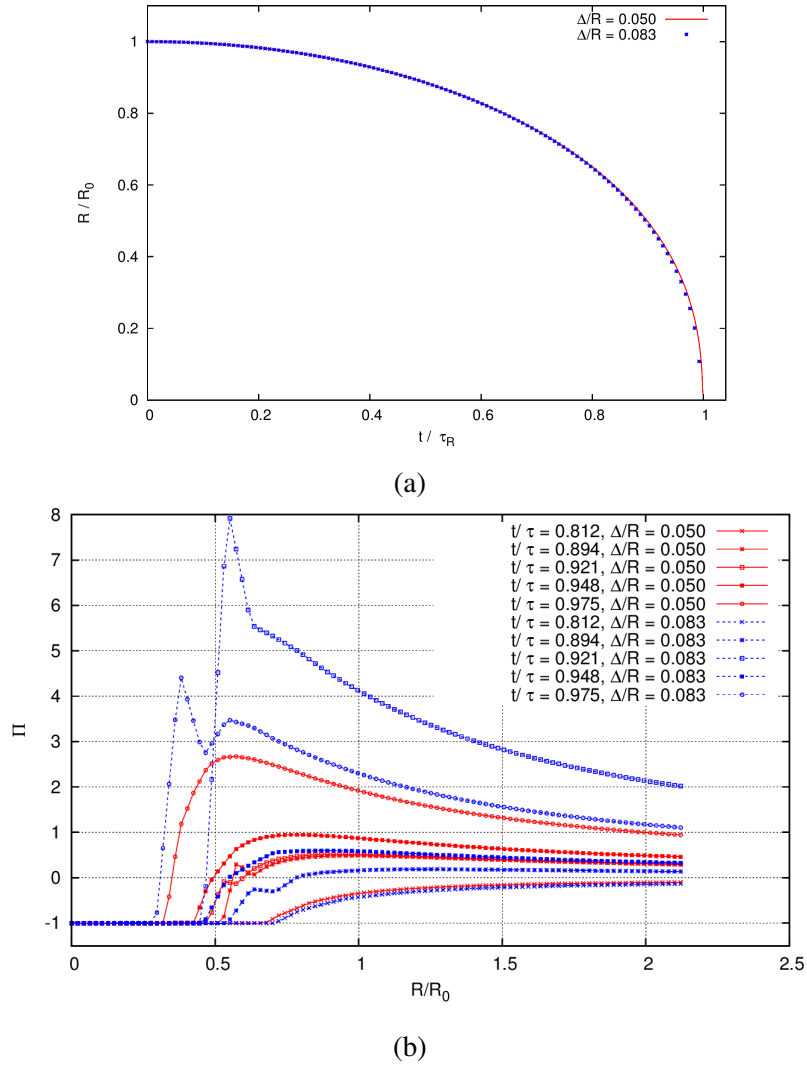**Figure 3.11**: Domain discretization effect on the finite mass transfer model; (a) bubble radius; (b) pressure profile

3.1.3 Lagrangian model result

In this section, first the Lagrangian results based on the original form of the R-P equation (2.30) are presented. In the original form of the equation, the farfield pressure is known and constant. In such case, since we have the exact development of bubble radius from the analytical solution (Equation 3.2), the vapour fraction field is resolved accurately and the result can be used to investigate the pressure equation and mass transfer rate. The problem is also solved based on the localized form of R-P equation (Equation 2.31) to investigate the effect of local pressure in calculation of bubble dynamics since the original form of R-P is not applicable in more complicated problems, as will be shown later.

In Figure 3.12, the obtained pressure profile from the Lagrangian approach with original R-P is compared with the analytical data for two different mass transfer coefficients. Similar to the Eulerian model, the coefficients should be high enough for an accurate estimation of pressure inside the bubble; however, even with small coefficients no numerical pulse is seen in the Lagrangian model results and the outside pressure profiles are very well estimated, Figure 3.12a. Also, for this model, one only needs to make sure that the coefficients are high enough and the pressure profiles are well captured even at the last stages of collapse, Figure 3.12b, and no considerable difference is seen when the empirical constants are increased further, Figure 3.12c. It should be mentioned that the solution instability problems, that were mentioned for the finite mass transfer model above, do not exist for this Eulerian-Lagrangian approach, even when increasing the model constants to very high values or decreasing the time step to smaller ones. It seems that for the bubble Rayleigh collapse with the stated assumptions, the issue with the finite mass transfer model is related to the scalar transport equation of vapour fraction. When the exact value of bubble radius is known at each time step and the interface is sharply captured, the pressure equation (continuity) is solved accurately and only the mass transfer rate should be high enough to compensate for the bubble inertia in the Rayleigh-Plesset equation that was simplified in finite mass transfer models.

The inherent issues with the original form of Rayleigh-Plesset equation are its dependency on the constant known farfield pressure and the assumption of unrestricted field around the bubble. In most practical applications, the bubble is surrounded by other cavity structures and local flow effects need to be considered. There are modified versions of the equation in literature in which the local flow pressure on the bubble interface, or near that, is used in the equation (instead of p_∞) and to compensate for this simplification some correction terms are added to the equation. For example, Hsiao et al. [65] suggested a slip velocity correction term based on the bubble-flow velocity difference. Also, Giannadakis [66] proposed another correction term based on local turbulence quantities. However, for this simple collapse problem, such modifications in the equation cannot improve the results as the flow velocity is very small and there is no turbulence in the symmetrical flow around the bubble. As a solution, the equation was re-derived here
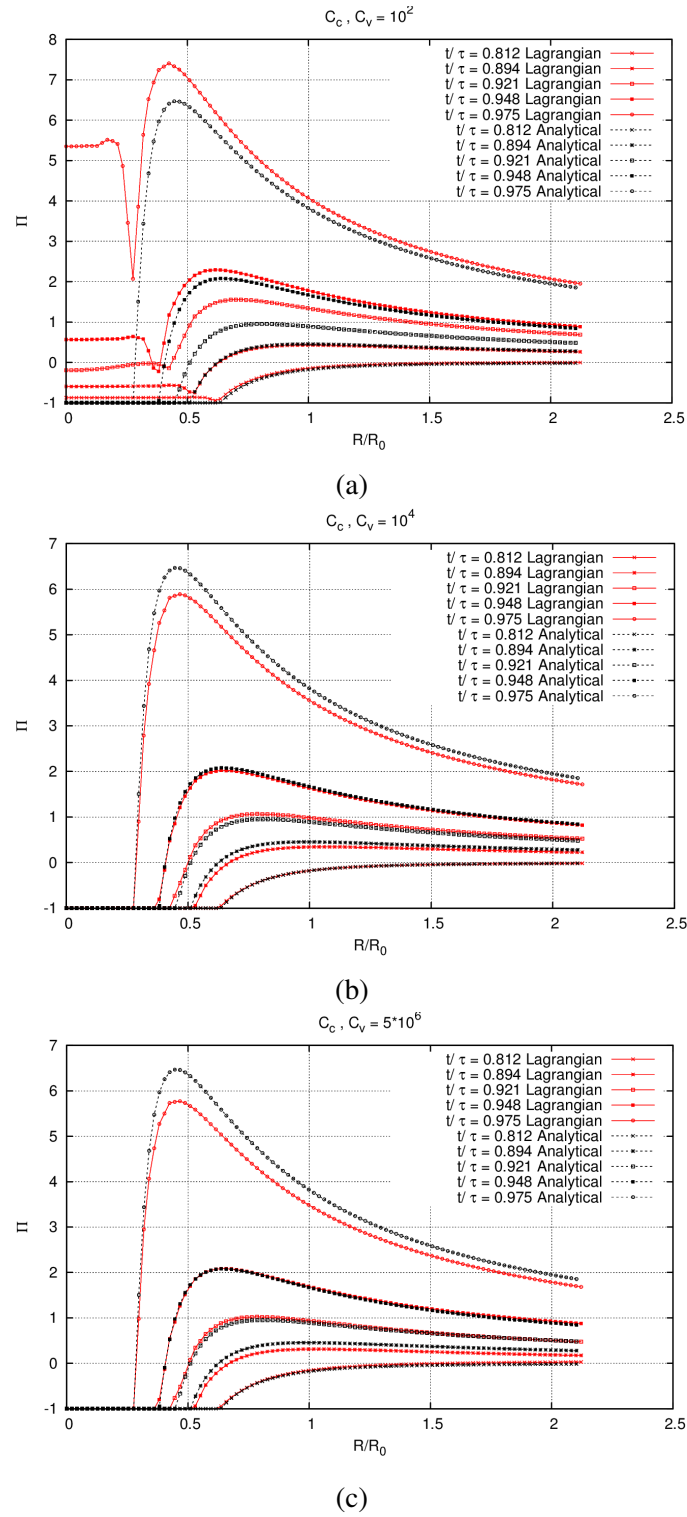
(a)

(b)

(c)

Figure 3.12: Comparison of Lagrangian model based on original R-P equation with analytical data in calculation of pressure distribution; (a) $C_c = C_v = 10^2$; (b) $C_c = C_v = 10^4$; (c) $C_c = C_v = 5 \times 10^6$

based on the local pressure value as stated before, using Equation 2.31.

In Figure 3.13, the Lagrangian model performance based on the localized R-P equation is validated with the analytical solution. Here, only the high coefficient ($C = 10,000$) result is presented, as the lower coefficients were shown to be problematic in pressure estimation inside the bubble, as discussed above. It is seen that the bubble radius evolution is well captured with the localized R-P as well. In Figure 3.14, the pressure lines for different time steps are compared with analytical solution which shows that this model can estimate the pressure peaks and their location with good accuracy and without any numerical pulse or significant delay in the pressure increase starting point. Only after $t/\tau_R > 0.95$ some discrepancy is seen between numerical and analytical data and it is due to the localized R-P equation dependency on the exact estimation of local pressure. During the last stages of the collapse, the pressure field around the bubble varies quite rapidly and a small error in pressure estimation can lead to considerable difference in bubble radius calculation which leads to more discrepancy in the following time steps. However, the estimated pressure in the last steps is still acceptable as compared to finite mass transfer and equilibrium models results.

In Figure 3.15, the results using a larger time step, $dt = 1 \times 10^{-7}$ s, are compared to the obtained data with $dt = 5 \times 10^{-9}$ s. The results are overall similar for bubble radius as well as pressure profiles and only in one time step ($t/\tau_R = 0.948$) the pressure line has a small shift.
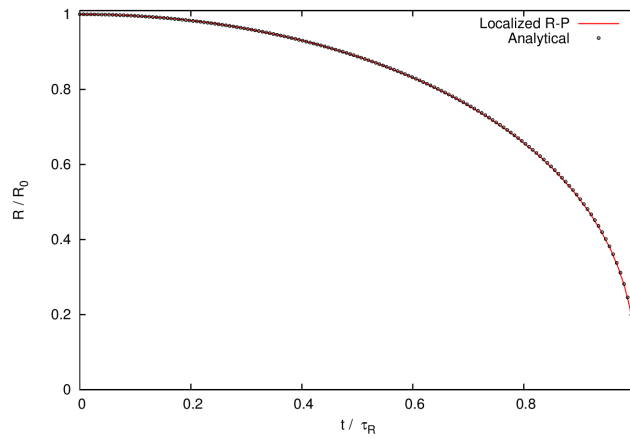
Figure 3.13: Validation of Lagrangian model based on localized R-P equation in predicting the evolution of the bubble radius

To study the model dependency on the grid resolution, the problem is solved with a coarser grid ($\Delta_r/R_0 = 0.083$) as well. In Figure 3.16, the calculated bubble radius and pressure profiles with empirical coefficients of 10^4 are compared with the corresponding ones of the fine grid and it is seen that even with coarser spatial discretization, the model has an acceptable accuracy and no numerical pulse is generated in the domain. It can be concluded that the Eulerian-Lagrangian model can produce satisfactory results with larger time steps and coarser grids as compared to other models.

Figure 3.14: Comparison of Lagrangian model based on localized R-P equation with analytical data

(a)

(b)

Figure 3.15: Time-step dependency of the Lagrangian model based on localized R-P equation; (a) bubble radius; (b) pressure profile

(a)

(b)

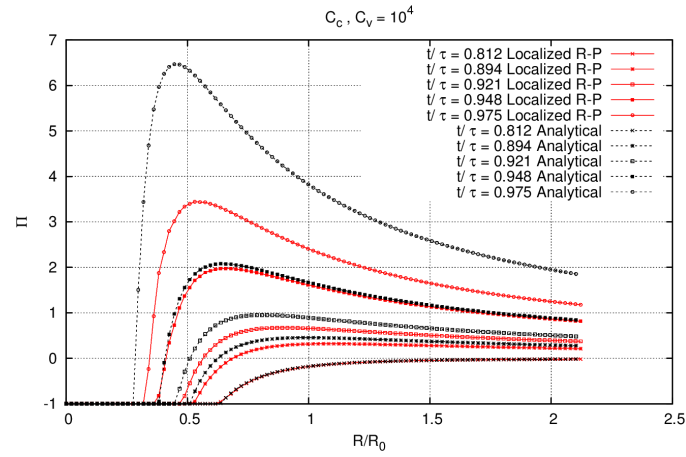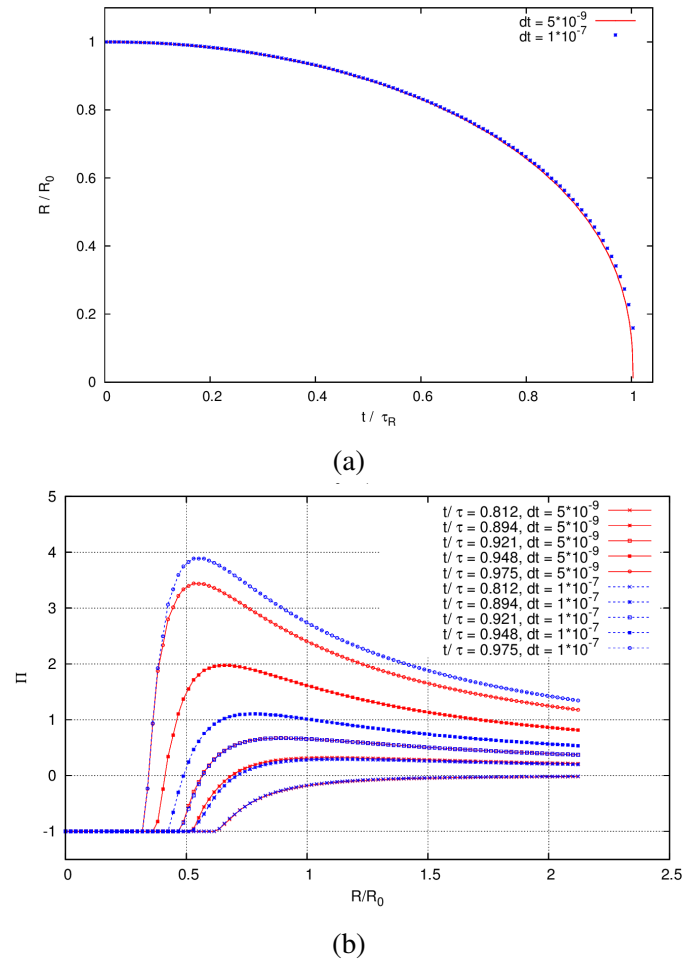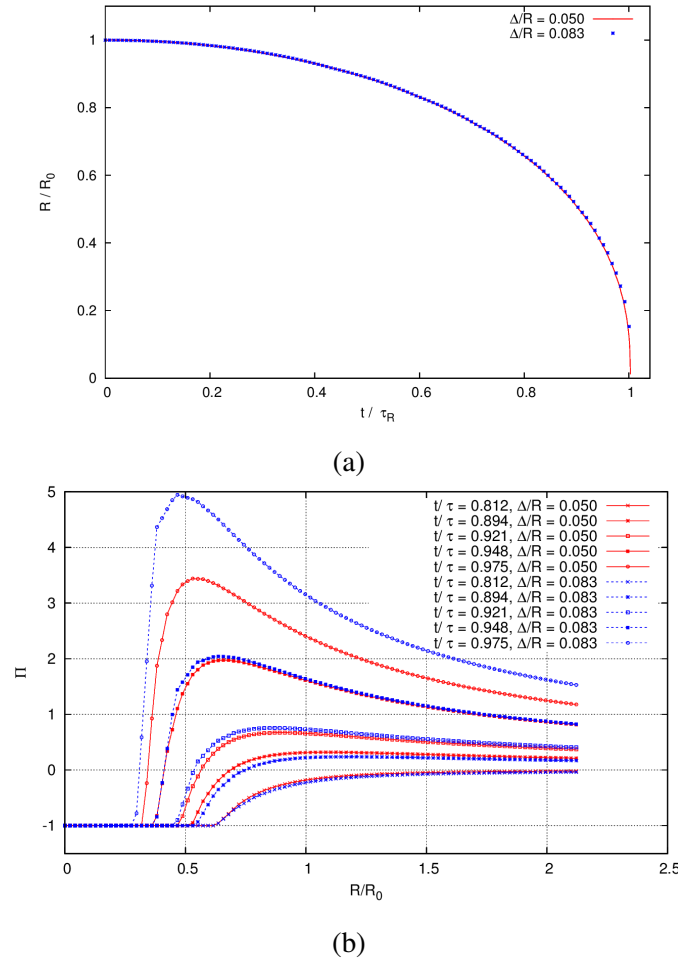**Figure 3.16**: Domain discretization effect on the Lagrangian model based on localized R-P equation; (a) bubble radius; (b) pressure profile

The single bubble collapse is a simple problem that can clarify the basic behaviour of the numerical approaches. However, the bubbles are usually surrounded by other cavity structures and the flow field can be restricted by wall boundaries. Also, there are special cases where the ambient pressure is so high that the observed numerical pulses are of minor importance and we are more interested in measuring large collapse pressures. In the following part, a more complex test case is simulated to analyse the models behaviour regarding these effects.

3.2 Collapse of a bubble cluster

In this section the collapse of a cluster of bubbles over a flat wall is simulated. Here, the bubble dynamics is affected by the collapse of the surrounding bubbles as well as the near wall influence. In the current study, the bubble cloud which was previously defined by Schmidt et al. [36] is used. This cloud consists of 125 spherical vapour bubbles with a radius distribution ranging from 0.70 mm to 1.64

mm with non-uniform distribution. The average radius of the bubbles is 0.95 mm and they have a minimum distance of 0.2 mm to avoid intersection. Also, they have larger concentration and radii around the center of the cloud. The overall cloud is located in a small liquid-filled cubic domain of $20 \times 20 \times 20$ mm^3 and has a total volume fraction of 5.8 %. The cubic domain, itself, is located in a larger rectangular domain of $4 \times 4 \times 2$ m^3 and the bottom faces of the two domains are coplanar. The bubble distribution inside the inner domain is depicted in Figure 3.17. Recently, Ogloblina et al. [67] investigated the bubble-bubble interaction and the stand-off distance effects on the collapse behaviour of the cluster and based on the obtained results, it can be concluded that the bubble interactions in the currently used cluster is significant.
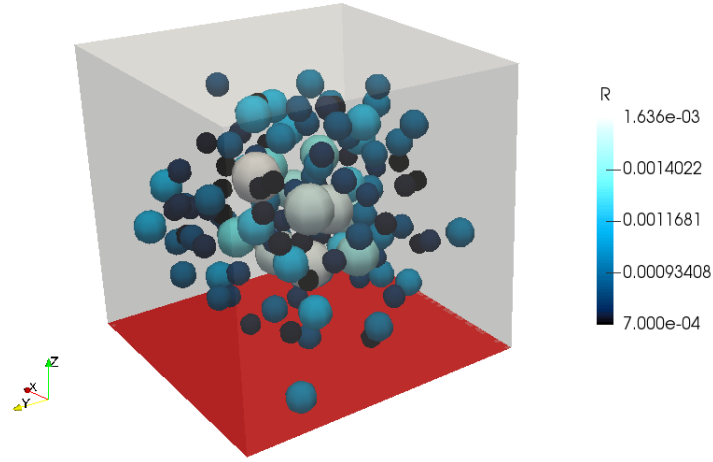

Figure 3.17: Distribution of 125 spherical non-intersecting bubbles within a cubic domain of 20^3 mm^3 over a flat wall (red surface). This domain is inside a large outer domain of $4 \times 4 \times 2$ m^3 (not shown here).

The fluid domain is assumed to have a stationary initial condition with a uniform temperature of 293 K. The initial pressure inside the bubbles is set equal to the vapour pressure of 2,340 Pa and in the surrounding liquid it is assumed to have a Laplacian distribution, which is reasonable for a stationary condition. The initial pressure along a line which passes through the cloud center is shown in Figure 3.18. The coplanar bottom faces of the domain are defined as impermeable walls and other outer faces are considered as far-field boundaries with constant pressure of 40 bar and no gradient of other flow quantities.

To discretize the bubble cloud, the small domain consists of uniform 55^3 cartesian structured cells with the numerical resolutions (Δ_{CFD}) of 0.36 mm, and it is equivalent to Grid 3 in the work of Schmidt et al. [3, 36]. In this discretization, the smallest bubbles are resolved by about 32 cells and the largest ones are discretized by more than 400 cells, which approximately corresponds to $0.2 < \Delta/R < 0.5$; it is thus coarse compared with the resolutions studied for the single bubble collapse. In Figure 3.19 the contours of the initial solution are shown. The vertical
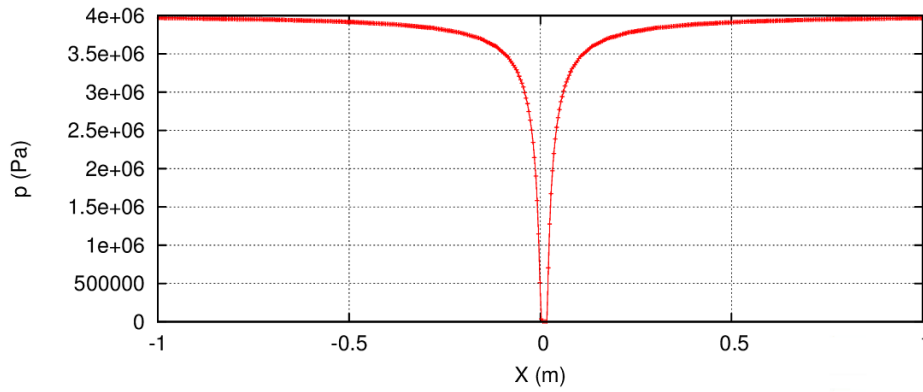
Figure 3.18: Initial pressure distribution along a line which passes through the center of the cloud. The line is defined as: -1 <x <1, y = z = 0.01.

cut planes are vapour fraction fields in the small inner domain using cell values (right) and continuous colouring (left), while the bottom horizontal face depicts the pressure field on the bottom face of the inner domain. In this figure, the upper limit of vapour fraction contours is set to 0.5 for better contrast.
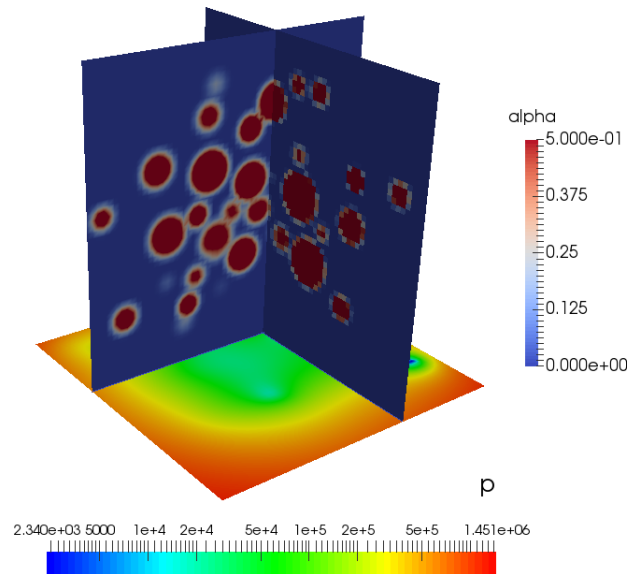
Figure 3.19: Initial flow contours for Grid3: vapour fraction using cell values (vertical right); vapour fraction using point values for continuous colouring (vertical left); pressure (horizontal)

The time step of the simulations is 3.9×10^{-8} s corresponding to CFL number (for compressible solution) of 0.7 and the sampling frequency of 2.56×10^7 Hz. For the pressure-velocity coupling of the finite mass transfer and Lagrangian models simulations, four outer SIMPLE loops are performed, and in each SIMPLE loop four PISO loops are performed. Finally, in order to measure the imposed

pressure of the collapsing bubbles on the bottom wall, one pressure transducer is located at the center of the bottom face. This transducer covers an area of $1 \times 1 \text{cm}^2$.

To validate the simulations, first the equilibrium model results are compared with the data of Schmidt et al. [3, 36]. In Figure 3.20a, the dimensionless volume variations of the bubble cloud and collapse durations are compared. As there is no experimental data or analytical solution for this specific cloud with the specified boundary conditions, a simplified analytical estimation is utilized to evaluate the general trend of the results. Assume the collapse of an *equivalent bubble* with the same initial vapour volume as the bubble cloud, yielding an initial equivalent radius of 4.8 mm. The Rayleigh collapse time of this bubble in a farfield pressure of 40 bar is 6.9×10^{-5} s (Equation 3.1). The collapse time of the numerical cloud in the current simulation is 7.3×10^{-5} s while from the work of Schmidt et al. [3] it is found to be 6.3×10^{-5} s. Therefore, both estimated collapse times are reasonable. The volume variation profile of the equivalent bubble is also plotted in Figure 3.20a for comparison. From the collapse time and volume variation profiles it is seen that there is a time shift between the two simulations. This shift is seen in the pressure profile as well, see Figure 3.20b. This is probably due to an anticipated small difference between the initial pressure field (resulting from solving the Laplace equation in the liquid) of the two simulations. However, the profiles look very similar for both volume variation and wall pressure, and after the initial shift the simulation profiles are almost parallel. There is also some difference in pressure peak values which is due to different flux schemes that were used in the simulations. In the pressure profile, the result of a finer grid ($\Delta_{CFD} = 0.09$ mm) is shown as well and it is seen that the results of the current study is more similar to the fine grid profile of Schmidt et al. [3].

In Figure 3.21, the vapour volume variations of the finite mass transfer model with different mass transfer coefficients are compared to the equilibrium model result. It is seen that with different mass transfer coefficients, the finite mass transfer model estimate similar variation for the total volume of the cloud with time. For the single bubble collapse, it was found that when the empirical constants are larger than a minimum value, the bubble radius profile does not show a considerable change. For a cloud of bubbles with a large ambient pressure (40 bar in this case), however, the total volume of the cloud does not change significantly with the chosen range of coefficient values, although individual bubbles may have different radius variations which can be anticipated from small differences between $C = 1$ profile and the others.

The temporal evolution of cloud volume for the Lagrangian model based on different R-P equations are compared to the equilibrium model in Figure 3.22. Three different forms of the R-P equation are used in these simulations. The first one is the original form of the equation (Equation 2.30) with the infinity pressure (p_∞) value equal to the pressure at the farfield boundaries (40 bar). The other case is the original form in which the liquid surface average pressure at the bubble interface is used as p_∞. As stated before, this approach has been used in literature

(a)

(b)
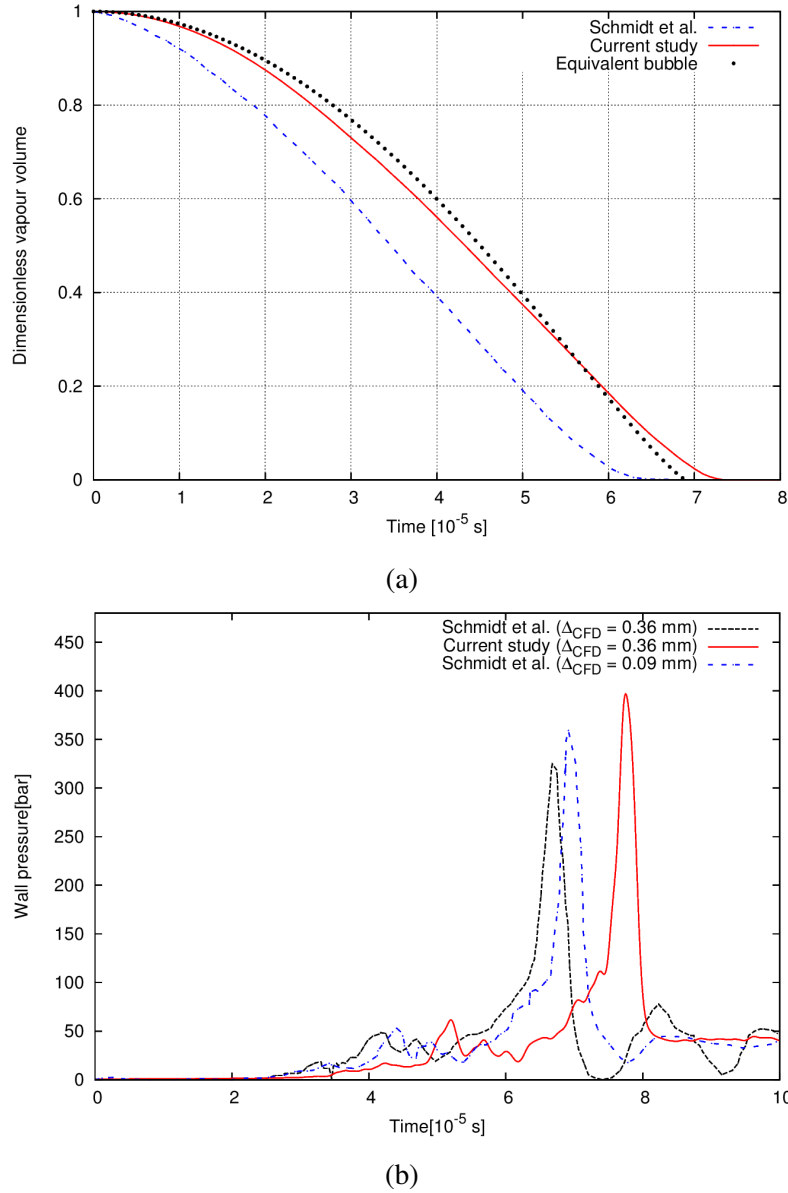
Figure 3.20: Validation of the equilibrium model simulation of bubble cluster; (a) time history of the vapour volume; (b) average pressure on the wall transducer

as a simplified method to consider local flow effect on the bubble. The third case is the localized R-P equation (Equation 2.31). It is seen in the figure that the original R-P equation with farfield pressure estimates a faster collapse. This is expected since the farfield pressure (40 bar) is much larger than the effective local pressure around the bubble. Also, replacing the farfield pressure with the corresponding value at the interface leads to a very slow rate of collapse and after 70 µs only 15 % of the cloud volume is condensed. In previous studies, this approach has been modified by correction terms such as a constant pressure added

Figure 3.21: Time history of bubble cloud volume using finite mass transfer model (FMT) with different coefficients

Figure 3.22: Time history of bubble cloud volume using Lagrangian model with different R-P equations

to p_∞, slip velocity correction term, [65], or corrections based on the turbulence quantities, [66]. However, such corrections do not work 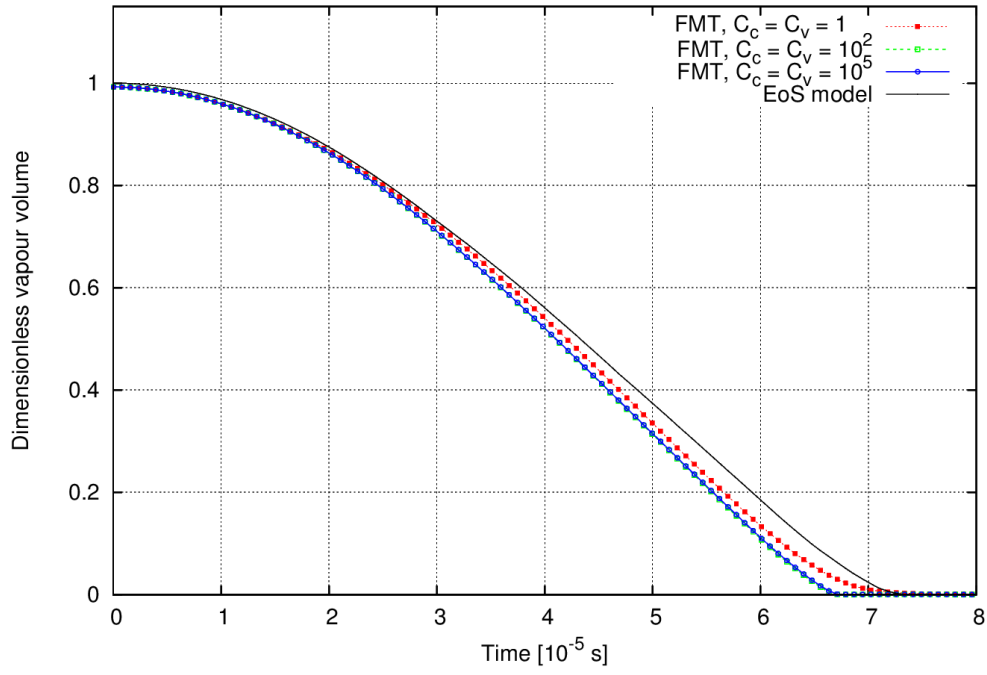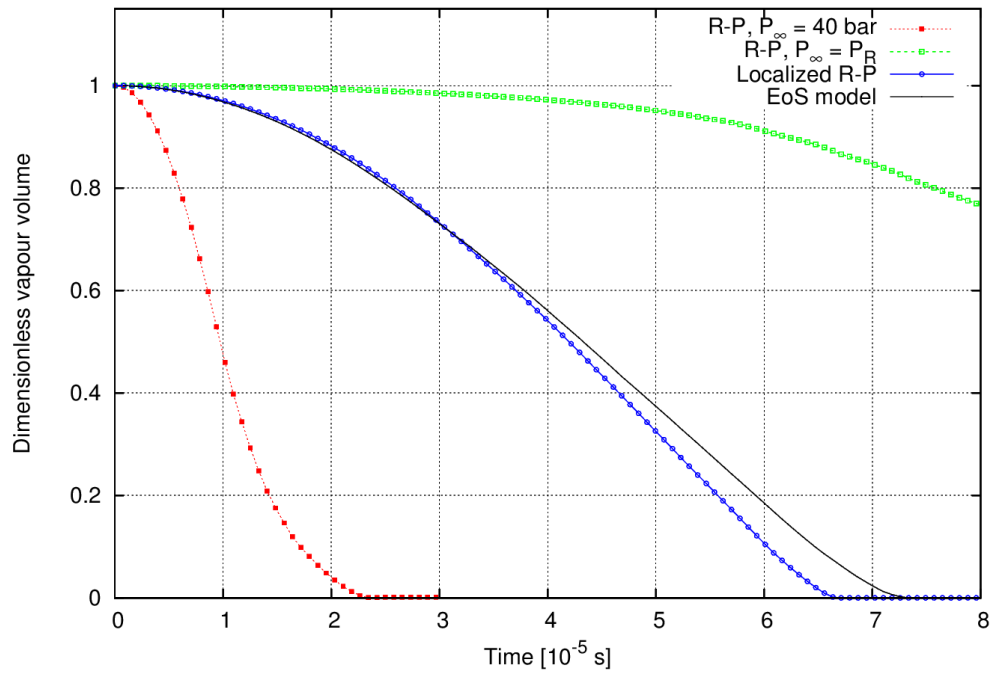for this problem, since the slip velocity and the turbulence level are negligible and the corrected constant pressure is unknown. Comparing to these two forms, the localized R-P equation can capture the collapse rate very well. In fact, the estimated collapse time is close to the one from equilibrium model and the total volume profile is very similar to the finite mass transfer method result, see Figure 3.21. It should be mentioned that for the localized R-P equation, the empirical constants should be larger than a minimum value ($C \approx 100$) to capture the volume profile reasonably. It is shown later that with smaller coefficients, the pressure field is not well-estimated and it affects individual bubble collapse in the Lagrangian approach. However, after this minimum value, the cloud rate of collapse is independent of the mass transfer coefficients.

In Figure 3.23, the average pressure profiles of the finite mass transfer models on the 1×1 cm^2 pressure transducer are compared with the equilibrium model result. For the single bubble collapse some numerical wiggles were detected in the pressure profiles of the equilibrium model results and as stated, in the polar grid, due to the simultaneous phase change in several polar cells (equidistant to the center), these wiggles are augmented and form larger pulses. In the bubble cluster case, however, a Cartesian grid is used and the numerical pulses are negligible compared to large physical collapse pressure peaks. In fact, no considerable numerical pulse is seen in the average pressure profile over the small transducer (Figure 3.20b) and the local peaks of the equilibrium model profile are related to the collapses of different bubbles. Therefore, the equilibrium model result can be considered a reasonable benchmark solution for estimation of the finite mass transfer model performance. In Figure 3.23, it is seen that the pressure estimation of the finite mass transfer model is highly dependent on the empirical coefficients, contrary to what was noted for the volume variation. If the coefficients are low, Figure 3.23a, no local pressure peak is seen from individual bubble collapse and the average pressure on the wall increases smoothly to the maximum value which corresponds to the final violent collapse, and after the collapse it decreases smoothly. When the coefficients are increased to moderate values of ($C = 10^2$), there are some local peaks in the wall pressure profile and the maximum pressure value is estimated much larger than the corresponding value of compressible equilibrium model, Figure 3.23b. When the coefficients are further increased to high values ($C = 10^5$), these peaks still exist, Figure 3.23c, and it is seen that for both moderate and high coefficients they are so frequent that the profile is not a regular line. It should be mentioned that the maximum pressure peaks for $C = 10^2$ and $C = 10^5$ are larger than 3000 bar which are not in the range of depicted plot. Actually, most of the local peaks can be regarded as spurious numerical pulses and it can be further distinguished if the plotted data are filtered out every 10 time steps as shown in Figure 3.24. From this figure, the finite mass transfer result for $C = 10^5$ is rather similar to the equilibrium model, although there is a time shift due to earlier collapse of the finite mass transfer approach. However, in general

cases that the correct solution is unknown, it is not possible to distinguish between numerical and physical collapse pulses and this can lead to inaccurate prediction of the impact loads and erosion estimations in cavitating flows.

In Figure 3.25, the average pressure profiles of the Lagrangian model with localized R-P equation are compared with the equilibrium model result. It is seen that with small mass transfer coefficients, the bubble cloud collapses too early and the model estimates too small local pressure peaks, Figure 3.25a. As shown in Figure 3.23a for the finite mass transfer model, when the empirical constants are small, the pressure field and its temporal peaks are not well captured. Since in the Lagrangian approach, the localized R-P solution is directly dependent on the surrounding pressure, an inaccurate pressure estimation leads to a wrong prediction of the vapour volume profile and collapse time. Also, for the larger coefficients, the estimated average pressures are similar to those of the finite mass transfer model, Figures 3.25b and 3.25c. It shows that even with more accurate formulation in resolving the vapour interface, the numerical pulses still exist. As stated before, in this study the compressibility of pure liquid and vapour are not taken into account and it seems that the liquid incompressibility around the cloud is the major reason for spurious pulses. In an incompressible fluid, every single pulse from the variation of a bubble size propagates simultaneously throughout the flow domain, including the wall boundary. Such numerical peaks can be seen in the work of Yakubov et al. [18], where ignoring the pure phase compressibility caused quite larger peaks in the hydrofoil surface pressure and lift force profiles (Figure 17 of [18]). However, considering the liquid compressibility in pressure based cavitating flow solvers may lead to ill-conditioned matrices of coefficients which needs special measures and smaller time steps to ensure solution stability and this, in turn increases the computational expenses; such an improvement is the subject of a future study.

For further comparison and understanding of different models, the bubble cloud structure and wall pressure contours at different time instances are depicted in Figure 3.26. It should be noticed that the time instances of different rows of the figure are not exactly the same. Since the equilibrium model result has a small time delay as compared to the other two models (Figs. 3.21 and 3.22) the time instances of the equilibrium model contours are chosen a little later $(0.2 - 0.4\,\mu s)$ to compare the corresponding instances of cavity structures in each row. Also, since there is a $0.2 - 0.4\,\mu s$ time difference in the collapse profile of the current equilibrium model results and the corresponding data of Schmidt et al. ([36]), the chosen time steps of Figs. 3.26c - 3.26e for the equilibrium model is exactly $1\,\mu s$ larger than the corresponding values in Figures 6(2)-6(4) of [36]. For plotting the cavity structures of the Eulerian models, the vapour fraction threshold of $0.01 < \alpha_v < 0.9$ is chosen. In Figure 3.26a, it is seen that while in the Lagrangian approach each spherical bubble can be presented with the exact dimension, in the Eulerian modelling the vapour volume is distributed over a number of cells which may lead to the diffusion of the bubble interface. For a more precise representation of bubble interfaces, a finer grid is needed as the one in the work of Schmidt et al.
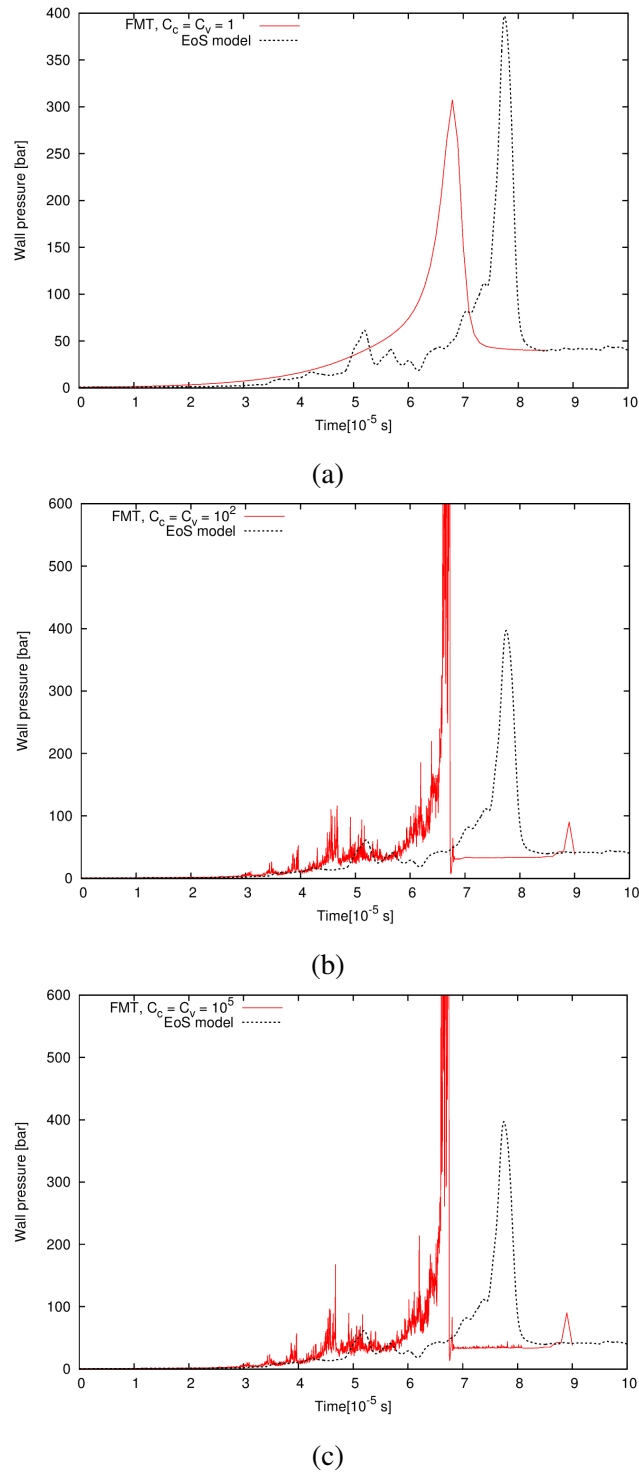
(a)

(b)

(c)

Figure 3.23: Average wall pressure over the small transducer using finite mass transfer model with different empirical constants; (a) $C_c = C_v = 1$; (b) $C_c = C_v = 100$; (c) $C_c = C_v = 10^5$
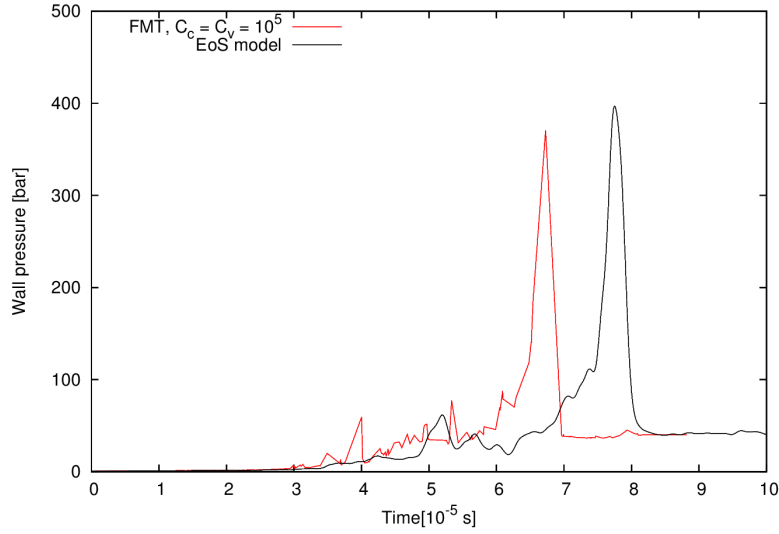
Figure 3.24: Filtered average wall pressure over the small transducer using finite mass transfer model with $C_c = C_v = 10^5$

[36] with 11 million cells in the inner domain or even, to have a better representation, the generated grid with a total of 120 million cells in the study of Adams and Schmidt [68]. Figure 3.26b is depicted to show the similarity in the cavity structures despite the difference in estimation of the pressure profiles between the compressible and incompressible methods. The small marked bubble in this figure collapse a few time step later and since it is close to the bottom boundary, the collapse pressure effect on the wall is considerable. Based on Figure 3.26c the equilibrium model can capture the emitted pressure wave on the wall as in this model the compressibility of the pure phases is taken into account. However, for the Lagrangian and finite mass transfer model the collapse pressure appears as a sudden and simultaneous pressure change in the whole flow domain (and not as an emitted wave). Therefore, no circular wave pattern is seen in the pressure contours of these models in which the liquid compressibility is neglected. In fact, the pressure on the wall, and specially close to collapse point, has a huge and instantaneous increase at the collapse time, but after just a few time steps the wall pressure becomes rather uniform.

Due to the nonsymmetrical pressure field around the bubbles, they are expected to lose their spherical symmetry during the collapse, as predicted by the equilibrium model. In fact, in the last steps of the collapse, the bubbles are deformed by impinging liquid jet and they are finally pierced and take a torus shape. However, as shown in Figure 3.26d for the Eulerian models, the bubbles have small deformation in shape while in the corresponding contours of [36] (Figure 6(3) of the paper) the small bubbles are already pierced by the liquid jet. The collapsing bubble have similar shapes later in Figure 3.26e, while in Figure 6(4) of [36] (the corresponding instance) the last bubbles have torus shape. Therefore, the Eulerian equilibrium model, at least, can estimate the bubble piercing

(a)

(b)

(c)
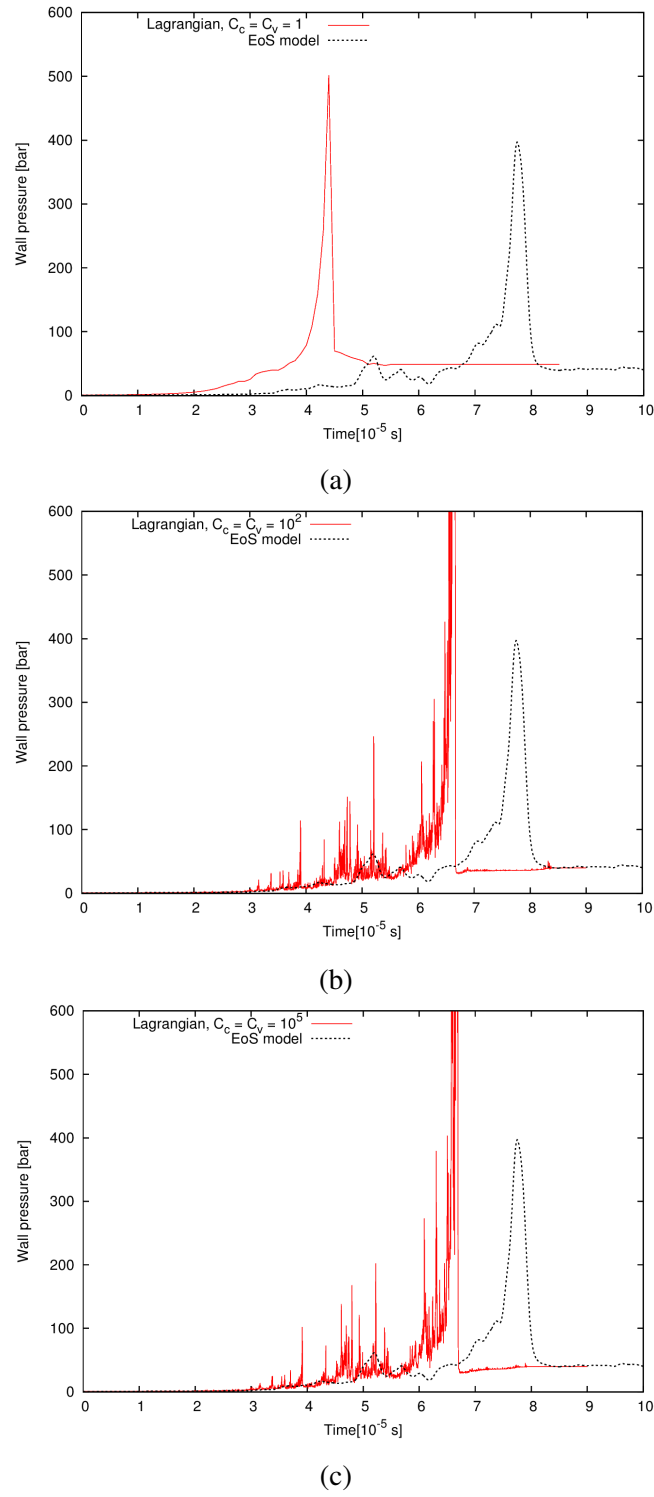
Figure 3.25: Average wall pressure over the small transducer using Lagrangian model with different mass transfer coefficients; (a) $C_c = C_v = 1$; (b) $C_c = C_v = 100$; (c) $C_c = C_v = 10^5$

(a)

(b)

(c)

(d)

(e)
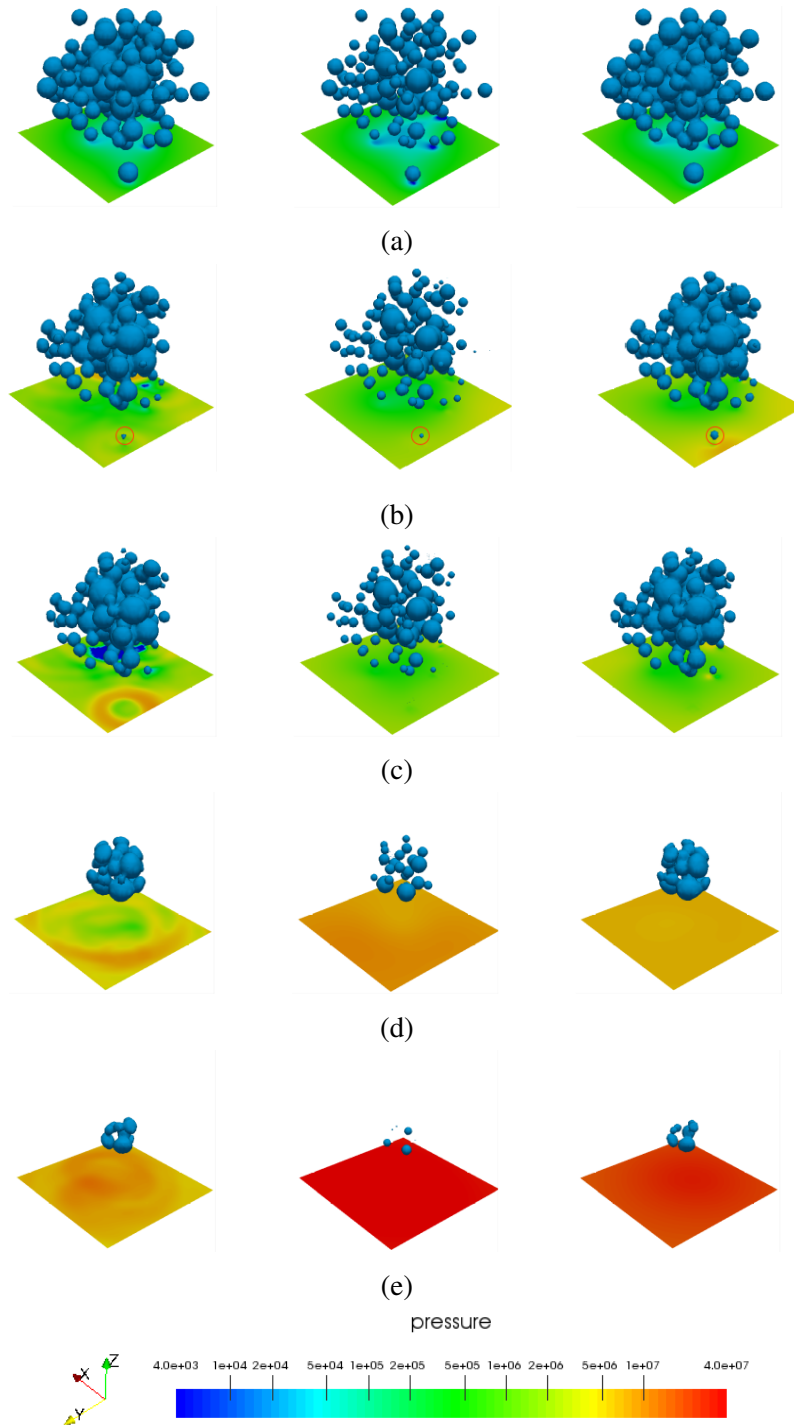
pressure

Figure 3.26: Comparison of equilibrium model (left), Lagrangian model (middle) and mass transfer model (right) in prediction of cloud structure and wall pressure at different time instances (a) $t = 0$; (b) $t = 3.4$ μs; (c) $t = 3.7$ μs; (d) $t = 6.1$ μs; (e) $t = 6.8$ μs.

and nonsymmetrical shapes, however it needs a very fine grid (around 220^3 cells for this case). From the middle contours of Figs. 3.26d and 3.26e, it is seen that the Lagrangian bubble stay spherical during the entire collapse time as in the Rayleigh-Plesset equation, the bubble is assumed to keep its symmetrical shape. However, it is possible to improve the Lagrangian model and consider the non-spherical shapes in this approach regardless of the computational grid size and it can be the subject of a future study.

3.3 Eulerian-Lagrangian transition in a 2D cavitating flow

In this section, the performance of the original and the new realizable Eulerian-Lagrangian models are compared during the Eulerian-Lagrangian transition process for qualitative validation of the proposed improvements (§2.4.2). In Figure 3.27a, two cavity structures with different length scales are shown over the suction side of a 2D hydrofoil. Following the transition criterion, the large structure should be kept in the Eulerian framework while the smaller one is a candidate to be transformed to the Lagrangian bubble framework. Also, in Figure 3.27b, the pressure contour around the cavities before transition is depicted. The contour is plotted on logarithmic scale for easier detection of pressure pulses. Inside the cavities (green area) the pressure is around vapour pressure (2340 Pa).

The pressure field after the Eulerian-Lagrangian transition of the original multi-scale model (i.e. without improvements) is shown in Figure 3.28. Figure 3.28a displays the pressure contour one time step after the transition. As can be seen, the local pressure at the small cavity location decreases to not only smaller than the threshold vapour pressure but also to large negative values. Also, some time steps later (Figure 3.28b), due to the decrease in pressure as well as the mass transfer source term in the α equation (Equation 2.15), new vapour structures are generated around the bubble which are subsequently transformed to new Lagrangian bubbles and leading to more pulses in the flow. Such spurious pulses are repeated several times in the domain.

The pressure contour obtained from the realizable model is shown in Figure 3.29. Here the small cavity structure is replaced by more but smaller bubbles in order to keep the $\alpha\beta$ parameter conserved during the transition. As a result, no numerical pulse or negative pressure is seen in the domain.

To have a better understanding, in Figure 3.30 the minimum pressure of the flow field is shown for 75 time steps after the Eulerian-Lagrangian transition. It is seen that while the minimum pressure of the realizable model is approximately constant and is around the threshold vapour pressure, for the original model, the pressure repeatedly yield large negative values due to several spurious pulses that occur after the transition. Such large negative pressures can influence the noise prediction and erosion estimation of a cavitating flow and if they occur near the hydrofoil, the hydrodynamic force estimation may be affected as well; in the worst case the numerical stability of the solver may be compromised. In Figure 3.31, the local vapour volume as well as the number of Lagrangian bubbles around the
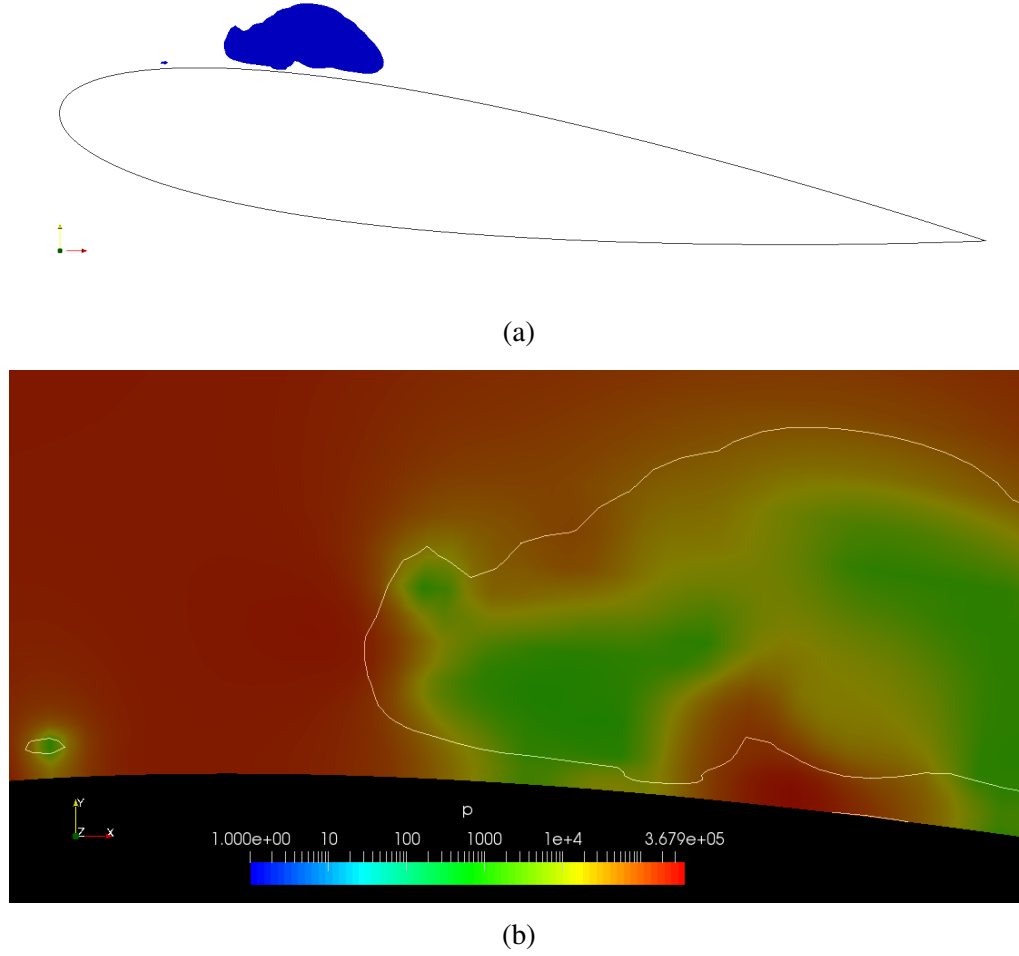
(a)

(b)

Figure 3.27: (a) Initial cavities with different length scales over a hydrofoil; (b) Initial pressure field, where the line indicates the iso-contour of vapour fraction $\alpha = 0.5$

transition area are depicted for 75 time steps after the transition. For the realizable model, the Eulerian-Lagrangian transition occurs once and after that no Eulerian vapour cavity is seen in the region and the number of bubbles stays constant. However, for the original model, new vapour cavities are generated in the area several times. As stated above, this vapour generation is due to the mass transfer source term in Equation 2.15 and the large negative pressure after each transition. As the new cavities are small, they are transformed to Lagrangian bubbles instantaneously which in turn leads to new spurious pulses and yet again vapour generation. Also, the number of Lagrangian bubbles increases in the domain. It should be noted that these bubbles are larger than the corresponding ones in the realizable model. The new bubbles increase the vapour content of the flow and interact with the earlier generated bubbles; both of these effects are unrealistic.

To show the overall performance of the improved multi-scale hybrid solver, the transport of various cavity structures over the 2D hydrofoil is shown in Figure
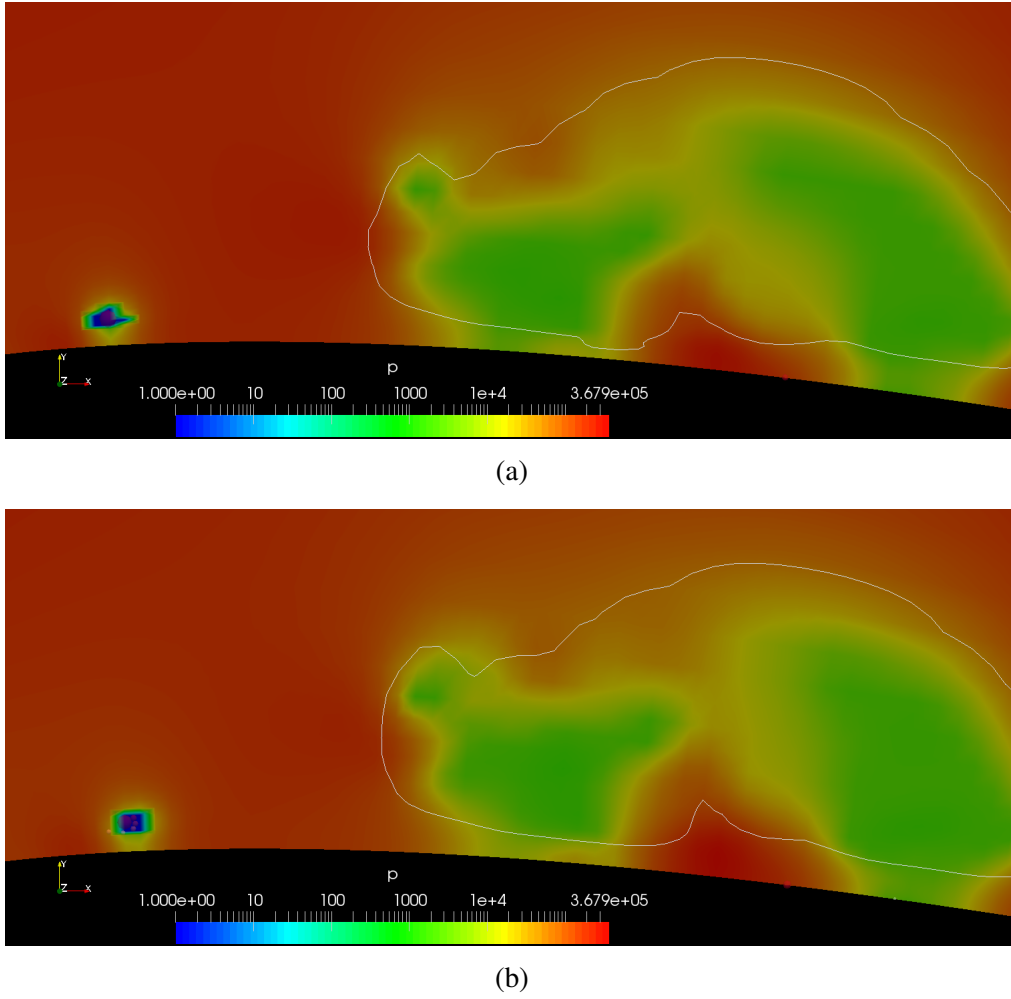
(a)

(b)

Figure 3.28: Pressure field (the line indicates the iso-contour of vapour fraction $\alpha = 0.5$) of the original model (a) one time step after transition; (b) a few time steps later

3.32 for a time period of about 1 ms. During this time period multiple transition of Eulerian cavities to Lagrangian bubbles and vice versa occur, and three of them are explained as examples. The two Eulerian cavities in Figure 3.32a, are the same structures of Figure 3.27a. As stated before, the smaller cavity, named *E1*, cannot be resolved by enough number of computational cells, and therefore it is transformed to the a group of Lagrangian bubbles. The bubbles are seen in Figure 3.32b, named as *L1* and enclosed by a dashed lined.

A few time steps later, Figure 3.32c, due to the surrounding pressure variations, a small part of the large Eulerian cloud, named *E2* is detached from the main part and starts to collapse. Meanwhile, a sheet cavity starts to develop at the leading edge of the hydrofoil. Also, a new group of Lagrangian bubbles are growing downstream of this structure, named *L3*. Later, the Eulerian sheet cavity develops further, and as it reaches the Lagrangian group (*L3*), the bubbles are
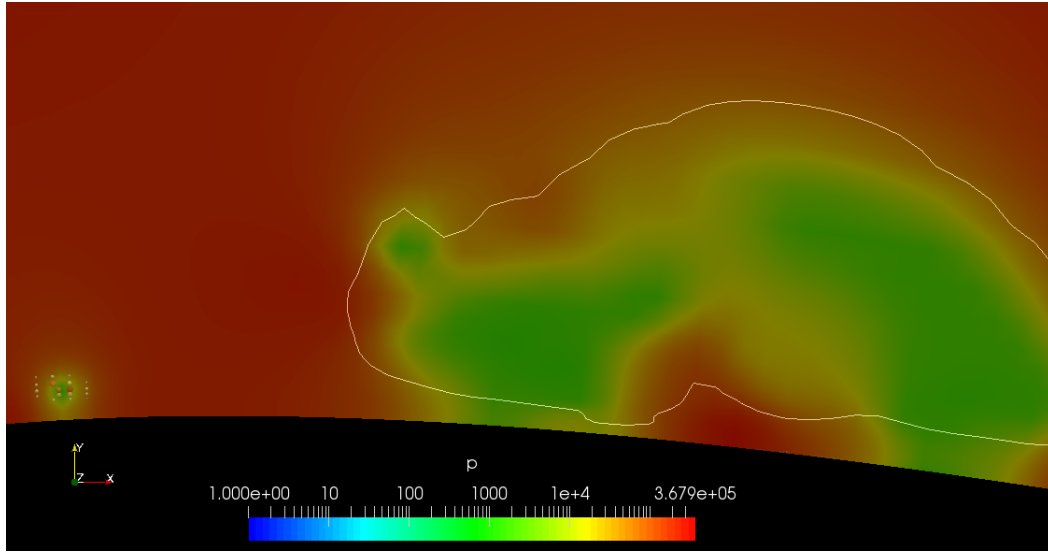
Figure 3.29: Pressure contour after the Eulerian-Lagrangian transition of the realizable model; the line indicates the iso-contour of vapour fraction $\alpha = 0.5$
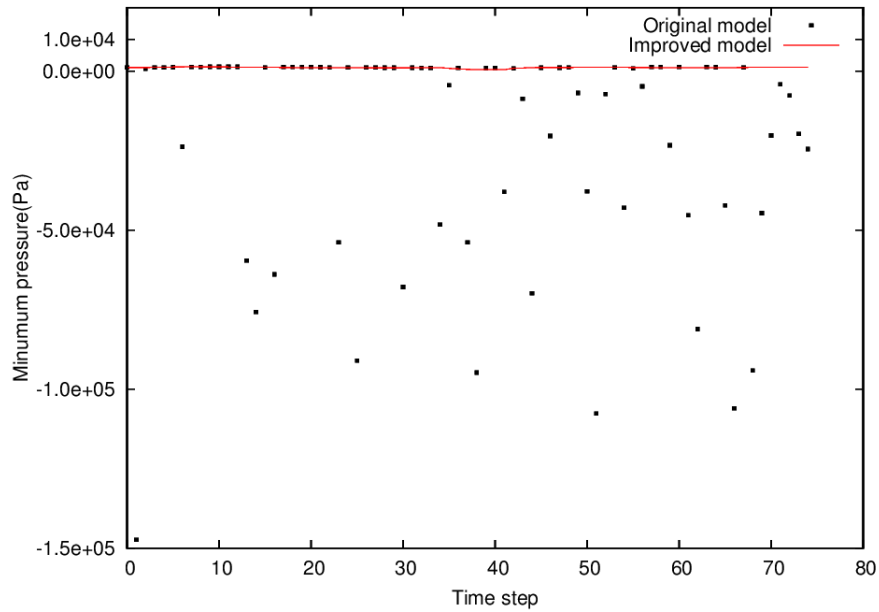
Figure 3.30: Minimum pressure after the first transition

transformed to Eulerian framework and become a part of the sheet cavity, since the combined cavity can be resolved by sufficient number of cells, Figure 3.32d. At the same time, the *E2* cavity continues its collapse and a smaller detached part of it is transformed to a bubble group. In Figure 3.32e, *E2* is completely transformed to the Lagrangian group of bubbles, *L2*. The *E2* cavity collapses at a fast rate, as the time interval between Figures 3.32d and 3.32e is about 2 μs. Finally,
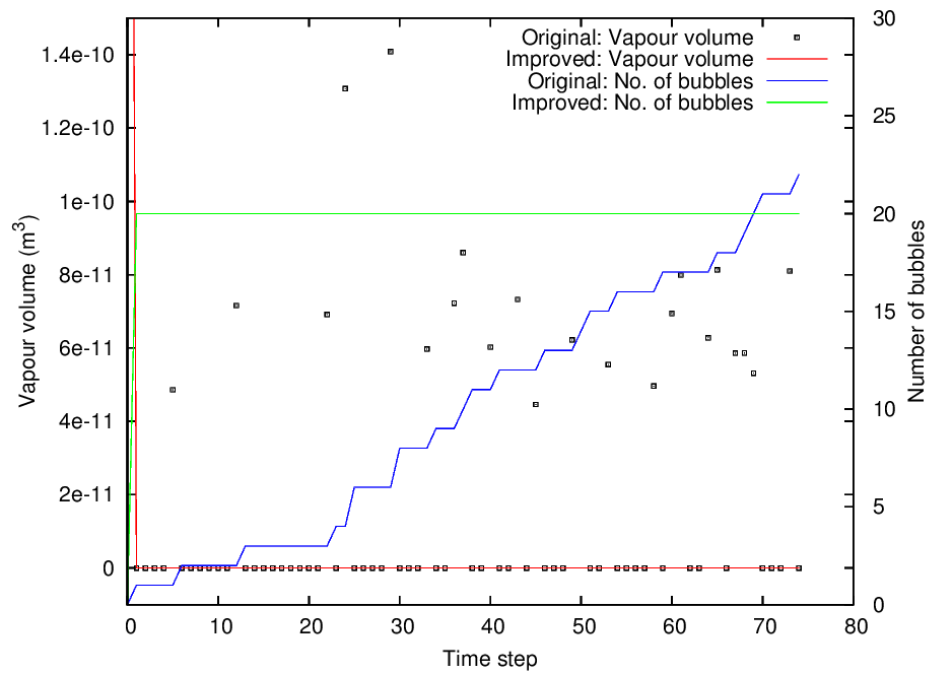
Figure 3.31: Vapour volume and number of bubbles after the first transition

in Figure 3.32f, it is seen that the old Eulerian cloud grows again and some of the Lagrangian bubbles of *L2* are transformed to Eulerian framework as they hit this cloud. Meanwhile, the leading edge sheet cavity develops further and absorbs more Lagrangian bubbles.
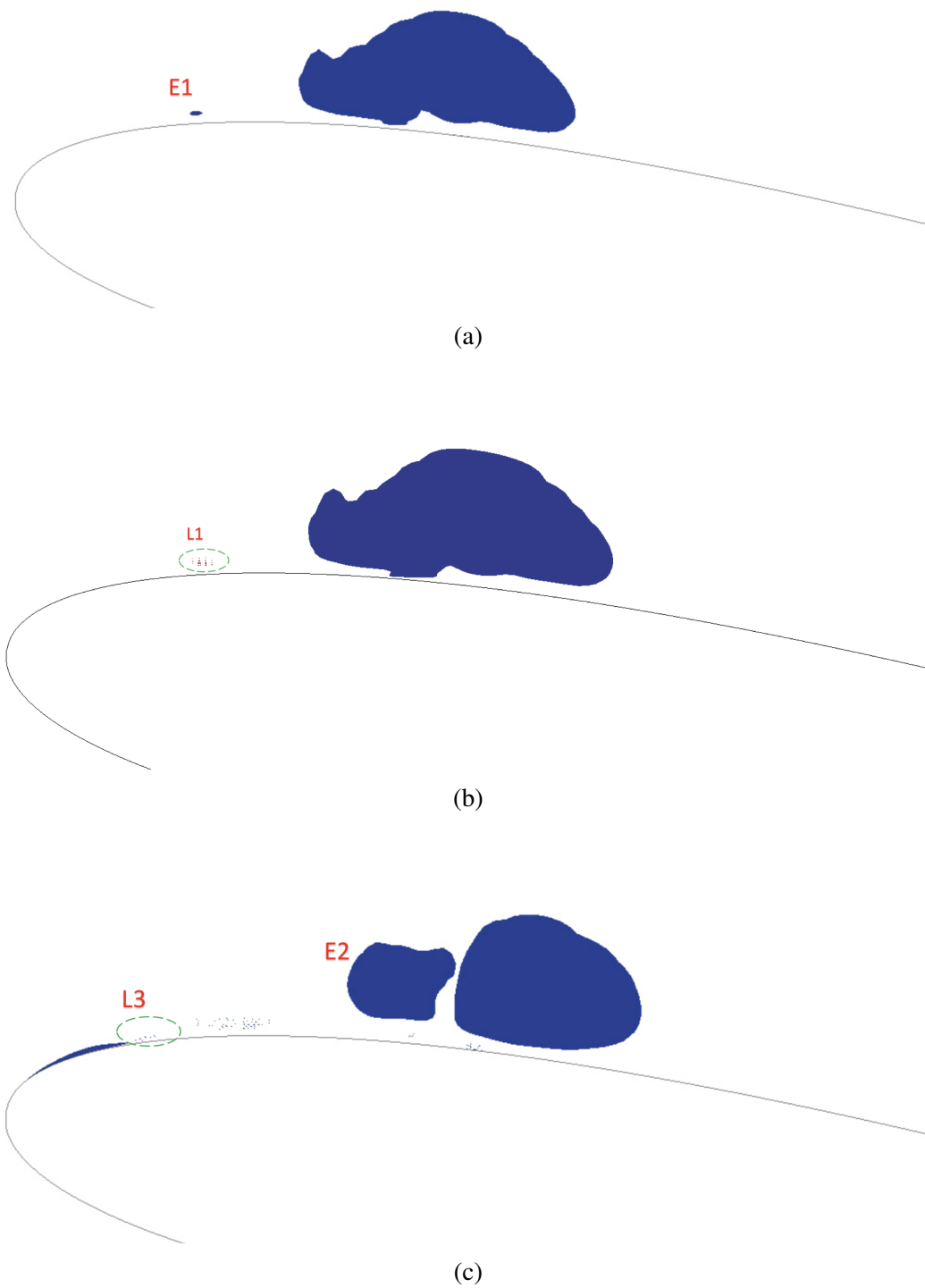
(a)

(b)

(c)

Figure 3.32: Eulerian-Lagrangian transition over a 2D hydrofoil

(d)

(e)

(f)
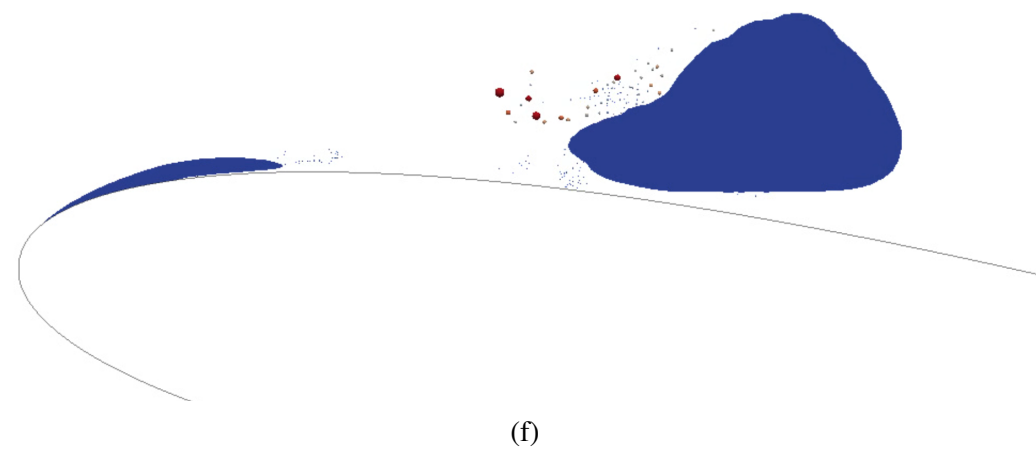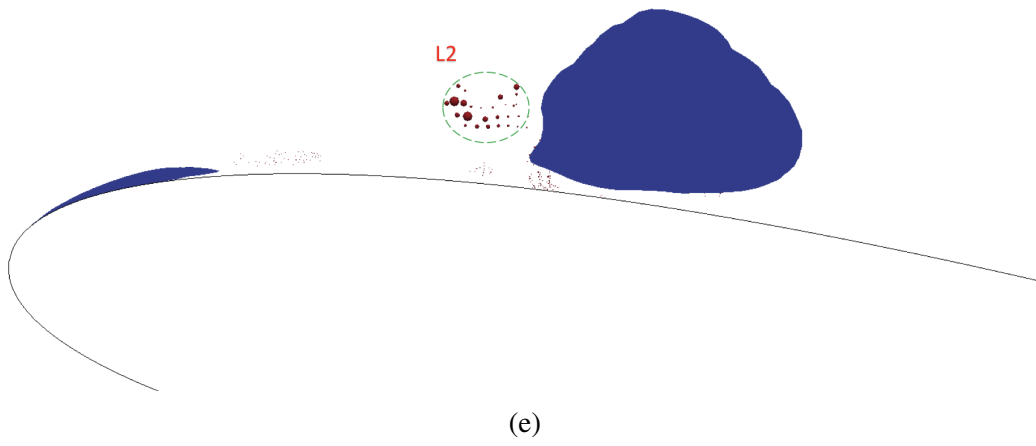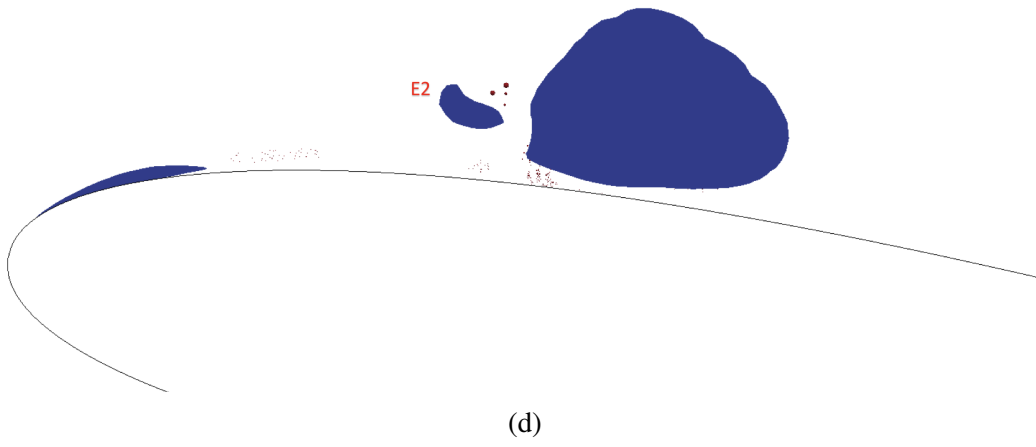
Figure 3.32: Eulerian-Lagrangian transition over a 2D hydrofoil (cont.)

4

Conclusions and future work

In this study, a hybrid mixture-bubble model in OpenFOAM was developed. This model is supposed to calculate cavitating flows with an extensive range of length scales from large sheet and cloud cavities to sub-grid micro bubbles. To understand the behaviour and limitations of different commonly used cavitation models and to find the potential area of improvements in the hybrid model, at first, three different cavitation models were compared in the simulation of two benchmark test cases. The models were the well established EoS and FMT models as well as a discrete bubble model that was implemented in the current study. From this comparison we conclude that:

- Eulerian models estimate a diffusive liquid-vapour interface and to have a more precise representation they need finer grids as compared to the Lagrangian model. The interface diffusivity can have considerable effect in the estimation of local pressure on the interface (as in the case of single bubble collapse) and the shape of cavity structure (as in the case of bubble cluster), especially in the last stages of the collapse.

- Some numerical pulses are detected in the estimated pressure profiles of the Eulerian models for the single bubble collapse problem, and this can be significant in collapse pressure calculation for special situations. From the comparison of the finite mass transfer and Lagrangian results, it is concluded that when the sharp bubble interface is estimated precisely, these numerical issues are solved.

- The numerical pulses are augmented when the grid lines are aligned with the bubble interface and there is a simultaneous phase change in several neighbouring cells. For the more complex case of bubble cluster, the Cartesian grid was used. Therefore, the pulses are not augmented, and they are negligible as compared to the high pressure in the farfield and large physical pressure peaks from individual bubble collapses.

- The Lagrangian models can give satisfactory results with larger time steps and coarser grids as compared to the Eulerian approaches.

Therefore, using a Lagrangian bubble model for the small scale cavity structures can reduce the computational cost through larger time steps and grid size, and at the same time improve the collapse pressure estimation around each single bubble.

Also, the Lagrangian bubble model was improved by derivation of a new form of the well-known R-P equation, in which the bubble size variation is calculated based on the local pressure value around the bubble. In the bubble cluster test case, the flow field around each bubble was unsymmetric and the correct estimation of the local pressure plays a more important role. It was shown in this case that using the local form of the R-P equation improves the model behaviour significantly. Other improvements of the bubble model include correcting the bubble-wall boundary condition in OpenFOAM as well as considering the bubble-bubble interaction on bubble dynamics. The other important parameter that causes difference in models behaviour is the fluid compressibility. From the bubble cluster test case, it was shown that considering the (pure phase) compressibility is effective in the estimation of the flow pressure and to have a reliable study of the cavity collapse pressure it is necessary to consider this parameter. However, from the comparison of the cavity structures of the compressible (EoS) and incompressible (FMT and bubble) models simulation, it is seen that even by ignoring the fluid compressibility, the collapse rate and vapour distribution can be predicted with reasonable accuracy. From this point, it can be concluded that the hybrid mixture-bubble model should be capable of representing the cavity dynamics even when ignoring the pure phase compressibility. However to calculate the erosion risk assessments, where the collapse pressure pulses are taken into account, either the liquid compressibility effect should be implemented in the model, or another erosion indicator based on the mixture and bubble dynamics should be implemented in the solver.

After understanding the characteristics of the models, the hybrid model was implemented in OpenFOAM by coupling the FMT mixture model with the Lagrangian bubble model. The initial implementation of the solver is similar to the earlier study of Vallier [35]. However, it was shown that using the initial algorithm leads to spurious numerical pressure pulses, as well as spurious vapour generations and insufficient consideration of bubble contribution in the mixture behaviour. Therefore, a remedy to these issues was presented by reformulating the coupling between the bubbles and the Eulerian governing equations to more accurately include the effects of bubbles on the Eulerian flow, as well as improving the Eulerian-Lagrangian transition algorithms. This amounts to considering the total vapour in the flow, and not only the Eulerian mixture vapour fraction. Also, the generation of Eulerian cavities in the bubbly cells was avoided by revising the source term of Eulerian vapour transport equation. In addition, during the Eulerian-Lagrangian transition process, several discrete bubbles are inserted to achieve a better representation of the spatial distribution of the Eulerian mixture

during the transition. Finally, the overall improvements were verified through a qualitative simulation of the 2D cavitating flow around a hydrofoil.

In future, the hybrid model will be improved further. The non-condensable gas effect will be implemented in the Lagrangian library. There are special problems in which the non-condensable gas content should be considered as it can be effective during the bubble collapse / rebound and implementing this parameter is expected to improve the hybrid model in the simulation of collapsing cavities. Also, the Eulerian-Lagrangian transition algorithm will be enhanced further to consider more flow physics, especially in complex real case problems. In some of the earlier developed hybrid models, a newly injected bubble is assumed to have a zero rate of collapse and to be in equilibrium condition with the surrounding liquid. However, as in our hybrid solver, a new bubble is a transformed Eulerian collapsing cavity, it has an initial rate of collapse that should be considered in initializing the $\dot{R}$ value in the R-P equation. Besides that, individual bubbles will be replaced by parcels to reduce the computational cost. In Lagrangian modelling, each parcel represents a group of bubbles and the parcel contribution in the mixture flow is similar to the contribution of the related bubble group. Therefore, instead of tracking a specific number of bubbles in each group, only a parcel of them is tracked which decreases the computational cost of the Lagrangian simulations considerably. Also, the multi-scale model performance will be verified quantitatively with real case cavitation phenomenon. For this purpose, the cavitating flow around a cylindrical bluff body is simulated numerically. Recently, the experimental tests of this problem have been done as a part of this PhD thesis, and the obtained results will be available in the near future. The tests include an extensive range of different conditions from cavity inception to fully developed cavitating flows, which provides a suitable test case for numerical model validations. Furthermore, it will be tried to extend the model applicability to be used in erosion risk assessment as well. It may be done by incorporation of the radiated acoustic pressure wave due to bubble collapse and rebound or implementing the liquid compressibility effect in the solver, but a certain approach in this regard has not been decided yet.

REFERENCES

[1] J-P. Franc and J-M. Michel. *Fundamentals of cavitation*, volume 76. Springer Science & Business Media, 2006.

[2] A. H. Koop. *Numerical simulation of unsteady three-dimensional sheet cavitation*. PhD thesis, University of Twente, 2008.

[3] S. J. Schmidt, M. S. Mihatsch, M. Thalhamer, and N. A. Adams. Assessment of erosion sensitive areas via compressible simulation of unsteady cavitating flows. In *Advanced experimental and numerical techniques for cavitation erosion prediction*, pages 329–344. Springer, 2014.

[4] G. H. Schnerr, I. H. Sezal, and S. J. Schmidt. Numerical investigation of three-dimensional cloud cavitation with special emphasis on collapse induced shock dynamics. *Physics of Fluids*, 20(4):040703, 2008.

[5] N. Kyriazis, P. Koukouvinis, and M. Gavaises. Numerical investigation of bubble dynamics using tabulated data. *International Journal of Multiphase Flow*, 93:158–177, 2017.

[6] P. Koukouvinis, M. Gavaises, A. Georgoulas, and M. Marengo. Compressible simulations of bubble dynamics with central-upwind schemes. *International Journal of Computational Fluid Dynamics*, 30(2):129–140, 2016.

[7] E. Goncalves, M. Champagnac, and R. Fortes Patella. Comparison of numerical solvers for cavitating flows. *International Journal of Computational Fluid Dynamics*, 24(6):201–216, 2010.

[8] A. K. Singhal, M. M. Athavale, H. Li, and Y. Jiang. Mathematical basis and validation of the full cavitation model. *Transactions-American Society of Mechanical Engineers Journal of Fluids Engineering*, 124(3):617–624, 2002.

[9] R. E. Bensow and G. Bark. Implicit les predictions of the cavitating flow on a propeller. *Journal of fluids engineering*, 132(4):041302, 2010.

[10] E. Lauer, X. Hu, S. Hickel, and N. A. Adams. Numerical modelling and investigation of symmetric and asymmetric cavitation bubble dynamics. *Computers & Fluids*, 69:1–19, 2012.

[11] G. H Schnerr and J. Sauer. Physical and numerical modeling of unsteady cavitation dynamics. In *Fourth international conference on multiphase flow, New Orleans, USA*, volume 1, 2001.

[12] C. L. Merkle, J. Feng, and P. E. O. Buelow. Computational modelling of the dynamics of sheet cavitation. In *Proc. of the 3rd Int. Symp. on Cavitation, Grenoble, France*, 1998.

[13] R. F. Kunz, D. A. Boger, D. R. Stinebring, T. S. Chyczewski, J. W. Lindau, H. J. Gibeling, S. Venkateswaran, and T.R. Govindan. A preconditioned navier–stokes method for two-phase flows with application to cavitation prediction. *Computers & Fluids*, 29(8):849–875, 2000.

[14] Y. Ye and G. Li. Modeling of hydrodynamic cavitating flows considering the bubble-bubble interaction. *International Journal of Multiphase Flow*, 84:155–164, 2016.

[15] P. Koukouvinis and M. Gavaises. Simulation of throttle flow with two phase and single phase homogenous equilibrium model. In *Journal of Physics: Conference Series*, volume 656, page 012086. IOP Publishing, 2015.

[16] P. Koukouvinis, M. Gavaises, O. Supponen, and M. Farhat. Numerical simulation of a collapsing bubble subject to gravity. *Physics of Fluids*, 28(3):032110, 2016.

[17] P. Koukouvinis, M. Gavaises, O. Supponen, and M. Farhat. Simulation of bubble expansion and collapse in the vicinity of a free surface. *Physics of Fluids*, 28(5):052103, 2016.

[18] S. Yakubov, T. Maquil, and T. Rung. Experience using pressure-based cfd methods for euler–euler simulations of cavitating flows. *Computers & Fluids*, 111:91–104, 2015.

[19] E. Giannadakis, M. Gavaises, and C. Arcoumanis. Modelling of cavitation in diesel injector nozzles. *Journal of Fluid Mechanics*, 616:153–193, 2008.

[20] M. Abdel-Maksoud, D. Hänel, and U. Lantermann. Modeling and computation of cavitation in vortical flow. *International Journal of Heat and Fluid Flow*, 31(6):1065–1074, 2010.

[21] S. Yakubov, B. Cankurt, T. Maquil, P. Schiller, M. Abdel-Maksoud, and T. Rung. Advanced lagrangian approaches to cavitation modelling in marine applications. In *MARINE 2011, IV International Conference on Computational Methods in Marine Engineering*, pages 217–234. Springer, 2013.

[22] C-T. Hsiao, J. Ma, and G. L. Chahine. Simulation of sheet and tip vortex cavitation on a rotating propeller using a multiscale two-phase flow model. In *Fourth Int. Symp. Mar. Propulsors, Austine, Texas, USA*, 2015.

[23] A. Tomiyama and N. Shimada. Two-fluid model with interface sharpening. *journal computational fluid Dynamics*, 9(4):418–426, 2001.

[24] G. Černe, S. Petelin, and I. Tiselj. Coupling of the interface tracking and the two-fluid models for the simulation of incompressible two-phase flow. *Journal of computational physics*, 171(2):776–804, 2001.

[25] L. Štrubelj and I. Tiselj. Two-fluid model with interface sharpening. *International journal for numerical methods in engineering*, 85(5):575–590, 2011.

[26] X. Jiang, G.A. Siamas, K. Jagus, and T.G. Karayiannis. Physical modelling and advanced simulations of gas–liquid two-phase jet flows in atomization and sprays. *Progress in Energy and Combustion Science*, 36(2):131–167, 2010.

[27] D. Kim, M. Herrmann, and P. Moin. The breakup of a round liquid jet by a coaxial flow of gas using the refined level set grid method. In *APS Division of Fluid Dynamics Meeting Abstracts*, 2006.

[28] M. Herrmann. A parallel eulerian interface tracking/lagrangian point particle multiscale coupling procedure. *Journal of Computational Physics*, 229(3):745–759, 2010.

[29] G. Tomar, D. Fuster, S. Zaleski, and S. Popinet. Multiscale simulations of primary atomization. *Computers & Fluids*, 39(10):1864–1874, 2010.

[30] Y. Ling, S. Zaleski, and R. Scardovelli. Multiscale simulation of atomization with small droplets represented by a lagrangian point-particle model. *International Journal of Multiphase Flow*, 76:122–143, 2015.

[31] H. Grosshans, R-Z. Szász, and L. Fuchs. Development of an efficient statistical volumes of fluid–lagrangian particle tracking coupling method. *International Journal for Numerical Methods in Fluids*, 74(12):898–918, 2014.

[32] H. Ström, S. Sasic, O. Holm-Christensen, and L. J. Shah. Atomizing industrial gas-liquid flows–development of an efficient hybrid vof-lpt numerical framework. *International Journal of Heat and Fluid Flow*, 62:104–113, 2016.

[33] C-T. Hsiao, J. Ma, and G. L Chahine. Multiscale tow-phase flow modeling of sheet and cloud cavitation. *International Journal of Multiphase Flow*, 90:102–117, 2017.

[34] J. Ma, C-T. Hsiao, and G. L. Chahine. A physics based multiscale modeling of cavitating flows. *Computers & Fluids*, 145:68–84, 2017.

[35] A. Vallier. *Simulations of cavitation-from the large vapour structures to the small bubble dynamics*. PhD thesis, Lund University, ISBN 978-91-473-517-8, 2013.

[36] S.J. Schmidt, M. Mihatsch, M. Thalhamer, and N.A. Adams. Assessment of the prediction capability of a thermodynamic cavitation model for the collapse characteristics of a vapor-bubble cloud. In *WIMRC 3rd International Cavitation Forum*. University of Warwick UK, 2011.

[37] E. Ghahramani, M. H. Arabnejad, and R. E. Bensow. Realizability improvements to a hybrid mixture-bubble model for simulation of cavitating flows. *Computers & Fluids*, 2018.

[38] OpenFoam. *The Open Source CFD Toolbox openfoam foundation. http://www. openfoam.com*, Accessed: 2018-01-15, 2018.

[39] H. G. Weller, G. Tabor, H. Jasak, and C. Fureby. A tensorial approach to computational continuum mechanics using object-oriented techniques. *Computers in physics*, 12(6):620–631, 1998.

[40] H. Jasak. *Error Analysis and Estimation for the finite volume method with applications to fluid flows*. PhD thesis, Department of Mechanical Engineering, Imperial College of Science, 1996.

[41] H. Rusche. *Computational fluid dynamics of dispersed two-phase flows at high phase fractions*. PhD thesis, Imperial College London (University of London), 2003.

[42] I. Sezal. *Compressible dynamics of cavitating 3-D multi-phase flows*. PhD thesis, Technische Universität München, 2012.

[43] R. Saurel and R. Abgrall. A multiphase godunov method for compressible multifluid and multiphase flows. *Journal of Computational Physics*, 150(2):425–467, 1999.

[44] R. Saurel, P. Cocchi, and P. B. Butler. Numerical study of cavitation in the wake of a hypervelocity underwater projectile. *Journal of Propulsion and power*, 15(4):513–522, 1999.

[45] W. Wagner and H-J. Kretzschmar. International steam tables-properties of water and steam based on the industrial formulation iapws-if97, 2008.

[46] M. H. Arabnejad, R. E. Bensow, and C. Eskilsson. Density-based compressible solver with equilibrium cavitation model in openfoam. *19th Numerical Towing Tank Symposium - NuTTS, At St Pierre d'Oleron, France*, 2016.

[47] C. Eskilsson and R.E. Bensow. A compressible model for cavitating flow: comparison between euler, rans and les simulations. In *29th Symposium on Naval Hydrodynamics, Gothenburg, Sweden*, 2012.

[48] V. Venkatakrishnan. Convergence to steady state solutions of the euler equations on unstructured grids with limiters. *Journal of computational physics*, 118(1):120–130, 1995.

[49] A. Asnaghi, A. Feymark, and R.E. Bensow. Improvement of cavitation mass transfer modeling based on local flow properties. *International Journal of Multiphase Flow*, 93:142–157, 2017.

[50] A. Asnaghi. *Computational Modelling for Cavitation and Tip Vortex Flows*. PhD thesis, Department of Mechanics and Maritime Sciences, Chalmers University of Technology, 2018.

[51] A. Asnaghi, O. Petit, and T. Lackmann. CFD with opensource software: inter-PhasChangeFoam tutorial. 2013.

[52] S. V. Patankar and D. B. Spalding. A calculation procedure for heat, mass and momentum transfer in three-dimensional parabolic flows. In *Numerical Prediction of Flow, Heat Transfer, Turbulence and Combustion*, pages 54–73. Elsevier, 1983.

[53] I. E. Barton. Comparison of simple-and piso-type algorithms for transient flows. *International Journal for numerical methods in fluids*, 26(4):459–483, 1998.

[54] A. Asnaghi. *Developing computational methods for detailed assessment of cavitation on marine propellers*. PhD thesis, Department of Shipping and Marine Technology, Chalmers University of Technology, 2015.

[55] A. A. Amsden, P.J. O'rourke, and T.D. Butler. Kiva-ii: A computer program for chemically reactive flows with sprays. Technical report, Los Alamos National Lab., NM (USA), 1989.

[56] R. Mei. An approximate expression for the shear lift force on a spherical particle at finite reynolds number. *International Journal of Multiphase Flow*, 18(1):145–147, 1992.

[57] C. E. Brennen. *Cavitation and bubble dynamics*. Cambridge University Press, 2013.

[58] M. S Plesset and A. Prosperetti. Bubble dynamics and cavitation. *Annual review of fluid mechanics*, 9(1):145–185, 1977.

[59] L. F. Shampine and M. W. Reichelt. The matlab ode suite. *SIAM journal on scientific computing*, 18(1):1–22, 1997.

[60] A_K. Chesters. Modelling of coalescence processes in fluid-liquid dispersions: a review of current understanding. *Chemical engineering research and design*, 69(A4):259–70, 1991.

[61] A.K. Chesters and G. Hofman. Bubble coalescence in pure liquids. In *Mechanics and Physics of Bubbles in Liquids*, pages 353–361. Springer, 1982.

[62] B. Podvin, S. Khoja, F. Moraga, and D. Attinger. Model and experimental visualizations of the interaction of a bubble with an inclined wall. *Chemical Engineering Science*, 63(7):1914–1928, 2008.

[63] R. Zenit and D. Legendre. The coefficient of restitution for air bubbles colliding against solid walls in viscous liquids. *Physics of Fluids*, 21(8):083306, 2009.

[64] S. Schenke and T.J.C. van Terwisga. Simulating compressibility in cavitating flows with an incompressible mass transfer flow solver. In *Proc. of the Fifth International Symposium on Marine Propulsors, smp17, Espoo, Finland*, volume 1, pages 71–79, 2017.

[65] C-T. Hsiao, G. L. Chahine, and H-L. Liu. Scaling effects on bubble dynamics in a tip vortex flow: prediction of cavitation inception and noise. *Dynaflow Inc. Rep. 98007-1NSWC*, 2000.

[66] E. Giannadakis. *Modelling of Cavitation in Automotive Fuel Injector Nozzles*. PhD thesis, Imperial College, University of London, 2005.

[67] D. Ogloblina, S. J. Schmidt, and N. A. Adams. Simulation and analysis of collapsing vapor-bubble clusters with special emphasis on potentially erosive impact loads at walls. In *Experimental Fluid Mechanics*, 2017.

[68] N. A. Adams and S. J. Schmidt. Shocks in cavitating flows. *Bubble dynamics and shock waves*, pages 235–256, 2013.